

NEWCASTLE UNIVERSITY

MMATH REPORT

Anomalous Diffusion of Point Vortices

Author:
Em RICKINSON

Supervisors:
Prof. Carlo F BARENGHI
Dr. Nick PARKER

May 2015

Abstract

The behaviour of quantised vortices in dilute-gas Bose-Einstein condensates is an area of considerable current interest. We explore the dynamics of a collection of vortices in an infinite domain through numerical simulations. We compare the suitability of several models, including the Gross-Pitaevskii model, for our problem, selecting a model based on a Hamiltonian description of vortex motion which allows us to simulate in excess of 100 vortices in an infinite region. The formation and rapid escape of vortex dipoles, and the diffusion of the unpaired vortices are observed. We suggest a link between the formation of dipoles and the diffusion of unpaired vortices, quantify the diffusion process, and give preliminary results concerning the effect of multiply quantised vortices on the diffusion process.

Contents

1	Introduction	3
1.1	Vortices	3
1.2	Motivation	4
1.3	Note on Terminology	5
2	Modelling	6
2.1	Comparison of Models	6
2.1.1	The Gross-Pitaevskii Model	6
2.1.2	Superfluid Hydrodynamic Equations	7
2.2	The Point Vortex Model	7
2.2.1	Derivation of Equations of Motion	8
2.2.2	Details of the Model	9
3	Numerical Methods	12
3.1	System Setup	12
3.1.1	Infinite Domain Setup	12
3.1.2	Periodic Domain Setup	12
3.2	Runge-Kutta Methods	15
3.3	Tests	16
3.3.1	Two-Vortex Interactions	16
3.3.2	Periodic Domain	16
3.4	Assessing Accuracy	17
3.4.1	Runge-Kutta-Fehlberg Methods	17
3.4.2	Autonomous Hamiltonian	18
3.5	Identifying Vortex Dipoles	20
4	Anomalous Diffusion	23
4.1	Standard Diffusion	23
4.1.1	The Diffusion Equation & Gaussian Solution in One Dimension	23
4.1.2	Random Walk Process	24
4.2	Subdiffusion & Superdiffusion	26
4.3	Diffusion of Point Vortices with Unit Circulation	27
4.3.1	Overall Dynamics	27
4.3.2	Dynamics of the Main Group	29
4.3.3	Dynamics of Escaping Dipoles	32
4.4	Diffusion of Point Vortices with Multiple Circulation	35

5	Conclusions & Future Work	38
5.1	Conclusions	38
5.2	Future Work	39
A	Butcher Tableaux of Selected Runge-Kutta Methods	41
	Bibliography	43

Chapter 1

Introduction

1.1 Vortices

Vortices, localised regions of vorticity (that is, infinitesimal rotation of the velocity field), are a characteristic feature of turbulence, and are present in a wide range of physical systems on a vast range of length scales.

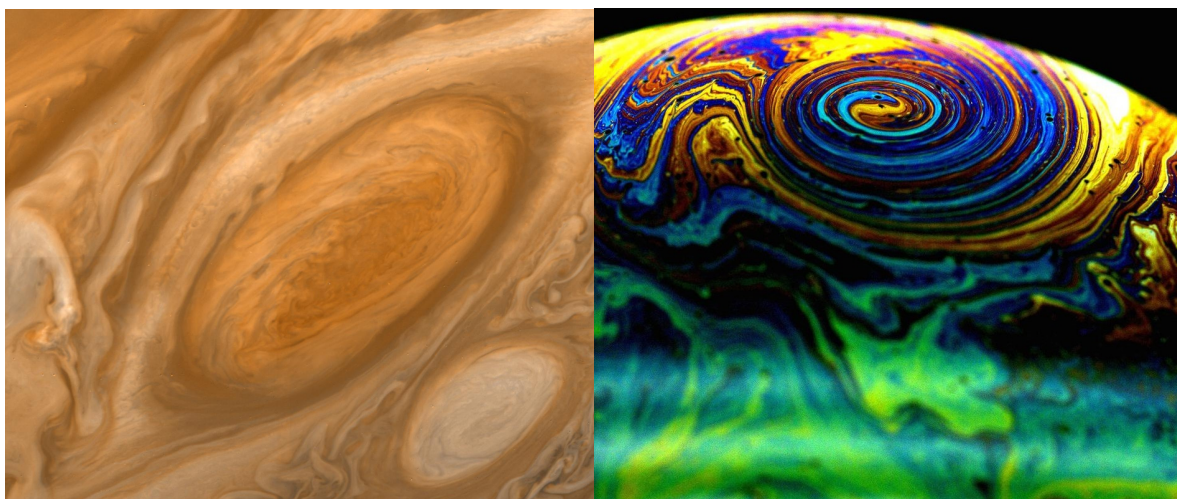


Figure 1.1: The ‘Great Red Spot’ in Jupiter’s atmosphere [1] (left) with length scale $\sim 10^7\text{m}$, and a vortex in a soap bubble film [2] (right) with length scale $\sim 10^{-2}\text{m}$.

As well as highlighting the range of length scales that classical vortices exist at, the systems in Fig. 1.1 can both be approximated as two-dimensional systems, as their extent in one direction is several orders of magnitude less than in the other directions. This approximation allows the use of the point vortex model, a two-dimensional model that treats vortices as singularities based on the work of Helmholtz (See [3] for a translation of the relevant work). Although this model is only applicable to idealised systems, and at the time was seen as something of a ‘toy’ model, in recent years it has garnered more interest, due to the theoretical prediction and experimental confirmation of an exotic state of matter: Bose-Einstein condensates.

Bose-Einstein condensation occurs when a dilute gas of bosons (particles with integer spin) are cooled to temperatures very close (usually within 10^{-7}K) to absolute zero. Such condensates are observed to be superfluid, and hence inviscid, and their ability to

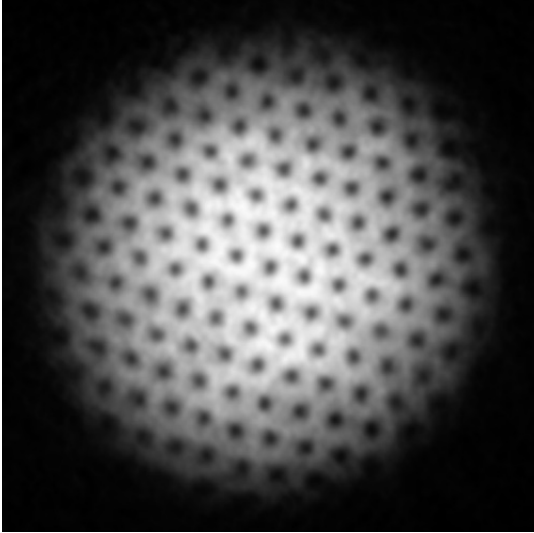


Figure 1.2: Vortex lattice in a trapped Bose-Einstein condensate [4]. Vortex cores are visible as dark regions corresponding to vanishing density.

support vortices is well documented experimentally, as in Fig. 1.2. The circulation, Γ , of vortices in superfluids is quantised, that is it can only take certain values:

$$\Gamma = \pm n \frac{\hbar}{m}, \quad n \in \mathbb{N}_+,$$

with m the mass of the boson in the condensate and \hbar the reduced Planck constant. Only vortices with $\Gamma = \pm\hbar/m$ are stable; vortices with larger circulation rapidly degenerate into multiple vortices with unit ($n = 1$) circulation. Moreover, these vortices have a microscopically small core structure, identical across all vortices. In this context some aspects of the point vortex model are no longer idealisations, but physically accurate. Indeed, recent experiments with vortices in condensates such as [5] have shown the point vortex model to give good agreement with the observed vortex dynamics.

1.2 Motivation

We consider the problem: given an initial configuration of quantum vortices (that is, vortices with quantised circulation) in an open region, will the region of turbulence spread out in space? To the best of our knowledge, nobody has tried to answer this question. It is easy to see that vorticity spreads out in classical fluids; the fluid motion of classical fluids is governed by the Navier-Stokes equation:

$$\frac{\partial}{\partial t} \mathbf{u} + (\mathbf{u} \cdot \nabla) \mathbf{u} = -\frac{1}{\rho} \nabla p + \nu \nabla^2 \mathbf{u}, \quad (1.1)$$

with \mathbf{u} the fluid velocity, p the pressure, ρ the density of the fluid, and ν the kinematic viscosity. The vorticity $\boldsymbol{\omega}$ is given by $\boldsymbol{\omega} = \nabla \times \mathbf{u}$. Taking the curl of equation (1.1):

$$\frac{\partial}{\partial t} \boldsymbol{\omega} = \nu \nabla^2 \boldsymbol{\omega} - \nabla \times [(\mathbf{u} \cdot \nabla) \mathbf{u}],$$

since the curl of a gradient is zero, and the curl commutes with the Laplacian operator and temporal derivatives. This is a (highly) nonlinear diffusion equation, implying that vorticity spreads. However, quantum fluids at sufficiently low temperatures are inviscid,

so the $\nu\nabla^2\omega$ term in (1.1) vanishes, and it is not clear how vorticity spreads out. The problem is motivated by the experimental ability to generate two-dimensional vortices in atomic Bose-Einstein condensates and observe their evolution, see, for example, [5].

1.3 Note on Terminology

Positive circulation corresponds to counter-clockwise motion about a vortex, and negative circulation corresponds to clockwise motion about a vortex. We will at points refer to vortices with negative circulation as anti-vortices or negative vortices, and to vortices with positive circulation as vortices or positive vortices. We use the terms ‘vortex’ and ‘vortices’ to refer both to vortices in general and vortices with specifically positive circulation; it should be clear which we mean in context.

A pair of vortices with opposite circulation and sufficiently small separation can, as detailed in Sec. 2.2.2, effectively act as a unit, following parallel trajectories. We refer to such pairs variously as ‘dipoles’, ‘pairs’, and ‘escaping pairs’.

Chapter 2

Modelling

2.1 Comparison of Models

We examine the suitability of various models for our investigation, that is describing the behaviour of a collection of quantum vortices, giving consideration to the aspects of vortex interaction they best capture, the computational intensity required to produce satisfactory - that is, quantitatively and qualitatively accurate - simulations, and the potential to extend to three-dimensions in future work.

2.1.1 The Gross-Pitaevskii Model

The (time dependent) Gross-Pitaevskii Equation (GPE) for describing the dynamics of a Bose-Einstein condensate is:

$$i\hbar\frac{\partial\Psi(\mathbf{r},t)}{\partial t} = \left[-\frac{\hbar^2}{2m}\nabla^2 + V(\mathbf{r}) + \frac{4\pi\hbar^2 a_s}{m}|\Psi(\mathbf{r},t)|^2 \right] \Psi(\mathbf{r},t), \quad (2.1)$$

where \hbar is the reduced Planck constant, m is the mass of the boson, V is the external potential, a_s is the scattering length, and Ψ is the wavefunction associated with the condensate as given in [6]. As a nonlinear partial differential equation (PDE) derived specifically as a quantum mechanical description of condensates - see [7] for one such derivation - the GPE is an obvious candidate as a model. It has distinct advantages: it models phonon emission, vortex core (hollow regions of size ξ , a quantity called the healing length) dynamics, and vortex-antivortex annihilation (that is, the mutual destruction of vortices over ranges comparable to the healing length), see references [8, 9].

As a PDE, numerical solutions involve the discretisation of a chosen region into a mesh, at every point of which Ψ and the relevant derivatives are evaluated in order to use a time-stepping technique to evolve the system. A suitably fine spatial and temporal resolution is required, with sufficiently small grid spacing and step size to capture the structure of the vortex core and its dynamics [10]. The equation can be solved in two- or three-dimensions as we please.

However, while the GPE has many desirable properties, the techniques required for producing numerical solutions render it a cumbersome option for our particular scenario. As we plan to investigate the spread of a considerable number of vortices through an infinite condensate, and have to consider the formation of high-velocity

pairs [9], we anticipate the need to simulate a large region in comparison to the region initially containing vortices, and thus an excessively large number of gridpoints, and we simply do not have the computational resources available to us to do so.

2.1.2 Superfluid Hydrodynamic Equations

As $\Psi(\mathbf{r}, t)$ is complex, it can be rewritten as $\sqrt{n(\mathbf{r}, t)}e^{i\theta(\mathbf{r}, t)}$, where $\theta(\mathbf{r}, t)$ is the phase of Ψ and $\sqrt{n(\mathbf{r}, t)}$ is the amplitude of Ψ , with $n(\mathbf{r}, t)$ the number density of bosons in the condensate which we can relate to the more conventional mass density ρ via $\rho = mn$. If we substitute this into (2.1) and separate out the real and imaginary parts we arrive at two superfluid hydrodynamical equations. The first is the continuity equation:

$$\frac{\partial n}{\partial t} = -\nabla \cdot (n\mathbf{u}),$$

where the fluid velocity \mathbf{u} is related to the phase of Ψ via:

$$\mathbf{u}(\mathbf{r}, t) = \frac{\hbar}{m}\nabla\theta(\mathbf{r}, t).$$

The second equation takes the form:

$$m\frac{\partial \mathbf{u}}{\partial t} = -\nabla \cdot \left(\frac{m\mathbf{u}^2}{2} + V + ng - \frac{\hbar^2}{2m\sqrt{n}}\nabla^2\sqrt{n} \right), \quad (2.2)$$

where g is an energetic cost associated with particle interactions, given by:

$$g = \frac{4\pi\hbar^2 a_s}{m},$$

with a_s the scattering length. For length scales less than the healing length and speeds less than Mach 1 (the local speed of sound), as discussed in Sec. 1.2 of [11], the quantum pressure term:

$$\frac{\hbar^2}{2m\sqrt{n}}\nabla^2\sqrt{n},$$

becomes negligible and (2.2) reduces to the Euler equation for an inviscid fluid from fluid dynamics. Although this allows us to interpret the condensate as a fluid, and makes it possible to visualise the condensate more directly, the Euler equation is also a PDE, and brings with it all of the disadvantages, in terms of computational intensity, outlined for the GPE.

2.2 The Point Vortex Model

Another hydrodynamical approach, the point vortex model (PVM) describes the velocity field around an embedded vortex in an idealised (incompressible, irrotational, inviscid) fluid plane [12]. Vortices are treated as point singularities, immediately dismissing the possibility of examining vortex core structure through this model. The equations of motion for the i^{th} of n such vortices consist of pairs of coupled nonlinear first-order ordinary differential equations (ODEs):

$$\frac{dx_i}{dt} = -\frac{1}{2\pi} \sum_{j=1}^n{}' \frac{\Gamma_j (y_i - y_j)}{r_{ij}^2}, \quad \frac{dy_i}{dt} = \frac{1}{2\pi} \sum_{j=1}^n{}' \frac{\Gamma_j (x_i - x_j)}{r_{ij}^2}, \quad (2.3)$$

where (x_i, y_i) is the position of the i^{th} vortex, Γ_i is the circulation, $r_{ij}^2 = (x_i - x_j)^2 + (y_i - y_j)^2$ is the separation of vortex i from vortex j , and the prime on the summation indicates the omission of the singular term $i = j$. For the sake of simplicity we take Γ to have integer values; if we wish to restore $\Gamma = n\hbar/m, n \in \mathbb{N}$ it is a simple matter of scaling. Although this model cannot be directly extended into three-dimensions, an analoguous model referred to as the vortex filament method exists, which treats vortices as filaments and makes use of the Biot-Savart Law to calculate the dynamics of the system, see for example pages 70-71 in [13].

2.2.1 Derivation of Equations of Motion

There are a number of ways to derive the point vortex model. Here we use equivalent geometric and algebraic methods to derive the equations of motion based on the fluid velocity around a point vortex.

The velocity around a vortex is entirely azimuthal, inversely proportional to the distance r from the vortex, and proportional to the constant circulation Γ around the vortex, such that $u_\theta = a\Gamma/r$ for some constant a , and $u_r = 0$. The circulation is given by:

$$\begin{aligned} \Gamma &= \oint_C \mathbf{u} \cdot d\vec{s} \\ &= \int_0^{2\pi} \frac{a\Gamma}{r} r d\theta \\ &= 2\pi a\Gamma, \end{aligned}$$

so $a = 1/2\pi$ to give $|\mathbf{u}| = u_\theta = \frac{\Gamma}{2\pi r}$. We illustrate this in Fig. 2.1. From this we can find u_x and u_y using a simple geometric argument:

$$u_x = -|\mathbf{u}| \sin \theta = -\frac{\Gamma}{2\pi r} \frac{y}{r} = -\frac{\Gamma y}{2\pi r^2}, \quad u_y = |\mathbf{u}| \cos \theta = \frac{\Gamma}{2\pi r} \frac{x}{r} = \frac{\Gamma x}{2\pi r^2}.$$

From an algebraic perspective, recall that in polar coordinates $|\mathbf{u}|^2 = \left(\frac{dr}{dt}\right)^2 + r^2 \left(\frac{d\theta}{dt}\right)^2$. As the velocity is completely azimuthal we have $\frac{dr}{dt} = 0$, which implies $|\mathbf{u}| = r \frac{d\theta}{dt}$. Then, using $x = r \cos \theta$:

$$\begin{aligned} \frac{dx}{dt} &= \frac{d}{dt}(r \cos \theta) \\ &= \cos \theta \frac{dr}{dt} + r \frac{d}{dt} \cos \theta \\ &= r \frac{d}{d\theta} \cos \theta \frac{d\theta}{dt} \end{aligned}$$

$$= -\sin(\theta)r\frac{d\theta}{dt},$$

where we have used the result $\frac{dr}{dt} = 0$. Using $\frac{y}{r} = \sin(\theta)$ and $r\frac{d\theta}{dt} = |\mathbf{u}|$:

$$\frac{dx}{dt} = -\frac{y}{r}|\mathbf{u}| = -\frac{\Gamma y}{2\pi r^2},$$

and similarly for dy/dt . Both of these derivations describe the velocity around a vortex at the origin; for a vortex at an arbitrary position (x_0, y_0) we let $x \rightarrow x - x_0$, $y \rightarrow y - y_0$ and arrive at:

$$\frac{dx}{dt} = -\frac{\Gamma(y - y_0)}{2\pi r^2}, \quad \frac{dy}{dt} = \frac{\Gamma(x - x_0)}{2\pi r^2}.$$

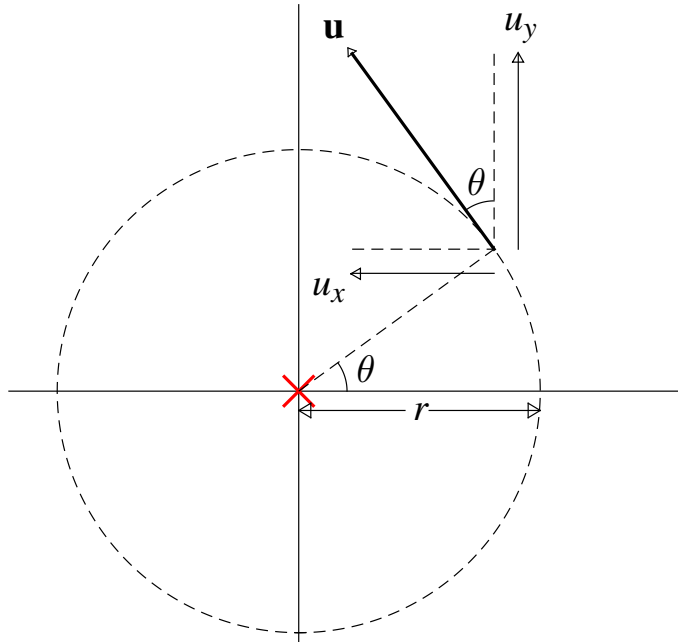


Figure 2.1: Direction of velocity at a point (r, θ) in the velocity field generated by a point vortex with positive circulation (red cross) at the origin.

This describes the fluid velocity around a vortex. This flow pattern can be associated with a stream function $\Psi = -\frac{i\Gamma}{2\pi} \ln z$ which satisfies Laplace's equation, so the velocity field due to an arbitrary number of vortices is given by the linear combination of the vortices' velocity fields. The full model (2.3) can then be reached with one final bit of information: the vortices are a material object [14], that is they move with the fluid (Helmholtz's second theorem of fluid dynamics).

2.2.2 Details of the Model

As the motion of the vortices is driven by the surrounding vortices, a solitary vortex will remain stationary. We consider two of the most basic interactions between quantised point vortices: configurations involving two vortices. First, the case where the vortices have equal circulation: $\Gamma_1 = \Gamma_2$. Let the vortices have positions (x_1, y_1) and (x_2, y_2) and velocities \mathbf{u}_1 and \mathbf{u}_2 . Then from (2.3) we have:

$$\begin{aligned}\mathbf{u}_1 &= \frac{1}{2\pi} \left(\frac{-\Gamma_2[y_1 - y_2]}{r_{12}^2}, \frac{\Gamma_2[x_1 - x_2]}{r_{12}^2} \right), \\ \mathbf{u}_2 &= \frac{1}{2\pi} \left(\frac{-\Gamma_1[y_2 - y_1]}{r_{21}^2}, \frac{\Gamma_1[x_2 - x_1]}{r_{21}^2} \right).\end{aligned}\tag{2.4}$$

Using $r_{21} = r_{12}$ and $\Gamma_1 = \Gamma_2$, we rewrite (2.4) as:

$$\mathbf{u}_2 = \frac{1}{2\pi} \left(\frac{\Gamma_2[y_1 - y_2]}{r_{12}^2}, \frac{-\Gamma_2[x_1 - x_2]}{r_{12}^2} \right) = -\mathbf{u}_1,$$

so the vortices have opposite velocities; their velocities are tangential to the line between the point vortices and they trace out a circular trajectory about their midpoint $([x_1 + x_2]/2, [y_1 + y_2]/2)$.

Now consider the case where the vortices have opposite circulation: $\Gamma_1 = -\Gamma_2$. Then:

$$\begin{aligned}\mathbf{u}_1 &= \frac{1}{2\pi} \left(\frac{-\Gamma_2[y_1 - y_2]}{r_{12}^2}, \frac{\Gamma_2[x_1 - x_2]}{r_{12}^2} \right), \\ \mathbf{u}_2 &= \frac{1}{2\pi} \left(\frac{-\Gamma_1[y_2 - y_1]}{r_{21}^2}, \frac{\Gamma_1[x_2 - x_1]}{r_{21}^2} \right).\end{aligned}$$

Using $r_{21} = r_{12}$ and $\Gamma_1 = -\Gamma_2$, we have:

$$\mathbf{u}_2 = \frac{1}{2\pi} \left(\frac{-\Gamma_2[y_1 - y_2]}{r_{12}^2}, \frac{\Gamma_2[x_1 - x_2]}{r_{12}^2} \right) = \mathbf{u}_1,$$

so their velocities are equal. The values of Γ_1 , Γ_2 , $x_1 - x_2$, $y_1 - y_2$ and r_{12}^2 are constant here, and so the pair move together in relative equilibrium. Note that the speed of their translation is inversely proportional to their separation.

Configurations involving more vortices exhibit less predictable behaviour, though both of these behaviours are observed within larger configurations when the separation within the pair is comparatively less than their separation from other vortices - we observe pairs of opposite circulation moving away from the main group of vortices with considerable speed.

In physical systems the annihilation of vortices of opposite circulation which become closer to each other than the healing length is observed, and the PVM as described here does not model this. In practice we can approximate these events by monitoring the separation between all vortices and removing at each time step any vortex-antivortex pairs with $r_{ij} \leq \xi$.

For pairs with the same circulation, inconsistency of the model with regard to the physical systems simulated has more to do with numerical accuracy, although the inability of this model to emulate phonon emission also contributes. As the speed of the vortices is inversely proportional to their separation, and such pairs in relative isolation trace out circles around their common center, a combination of small separation and insufficiently small step size leads to such a path being approximated by just a few time steps, inducing gross numerical errors; this applies to any tightly curved trajectories. This does not just apply to vortices with $r_{ij} \sim \xi$; the answer to ‘how close is too close?’ is particular to the numerical method and step size used, and the accuracy required.

One method to avoid this second pitfall is to impose a Rankine vortex velocity profile, displayed in Fig. 2.2, where the angular velocity remains unchanged at distances greater than some parameter a , and is proportional to r for distances less than a (see, e.g., [15]):

$$V_{\theta}(r) = \begin{cases} \Gamma r / (2\pi a^2), & r \leq a, \\ \Gamma / (2\pi r), & r > a. \end{cases}$$

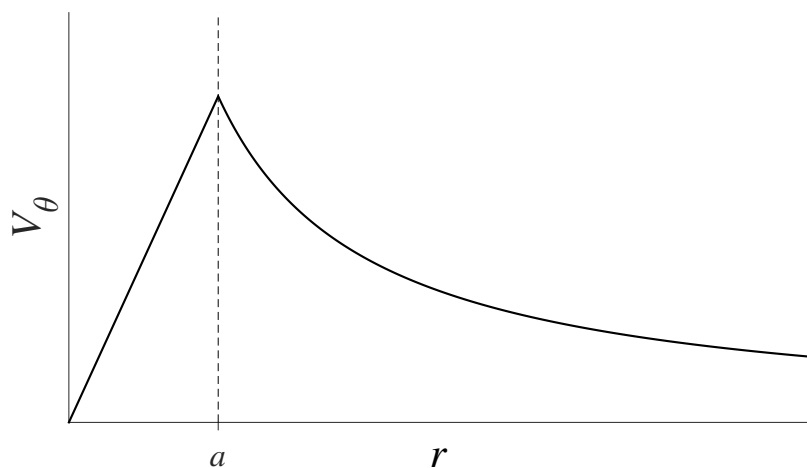


Figure 2.2: Typical velocity profile of a Rankine vortex.

We return to the implications of these techniques in Sec. 3.4.2.

Chapter 3

Numerical Methods

Without delving too deeply into the realm of the philosophy of science, when we simulate some reality it is worth bearing the ‘map-territory relation’, as discussed in [16], in mind. In all but the simplest cases, we have something of a play-off between simplicity and accurately corresponding to reality - the perfectly accurate map is the territory; the perfectly accurate simulation is the experiment. As we naturally find ourselves directed towards simplifications to be able to make progress with simulations, it is vital that we achieve accuracy where possible by careful consideration of numerical methods.

3.1 System Setup

Before focusing on the methods we detail the systems which we will be simulating.

3.1.1 Infinite Domain Setup

We initially work in an infinite plane in which we place 250 vortices, half with positive circulation and half with negative circulation for a net circulation of 0, at random locations within a disc of radius 1, which we visualise (with fewer vortices) in Fig. 3.1. The vortices are observed to spread out with no intrinsic preferred direction - that is, individual simulations may have preferred directions due to the randomness of the initial configuration, but over many simulations no preferred direction is apparent. We aim to investigate this ‘diffusion’, and so as to simplify matters we work to limit the spread of vortices to one dimension.

3.1.2 Periodic Domain Setup

We restrict the spread of vortices to one dimension by working in a domain which is periodic in one dimension (we arbitrarily choose the y -direction), and initially placing the vortices in a vertically-aligned strip with $-0.5 \leq x \leq 0.5$, $0 \leq y \leq 5$, as shown in Figs. 3.2 and 3.3.

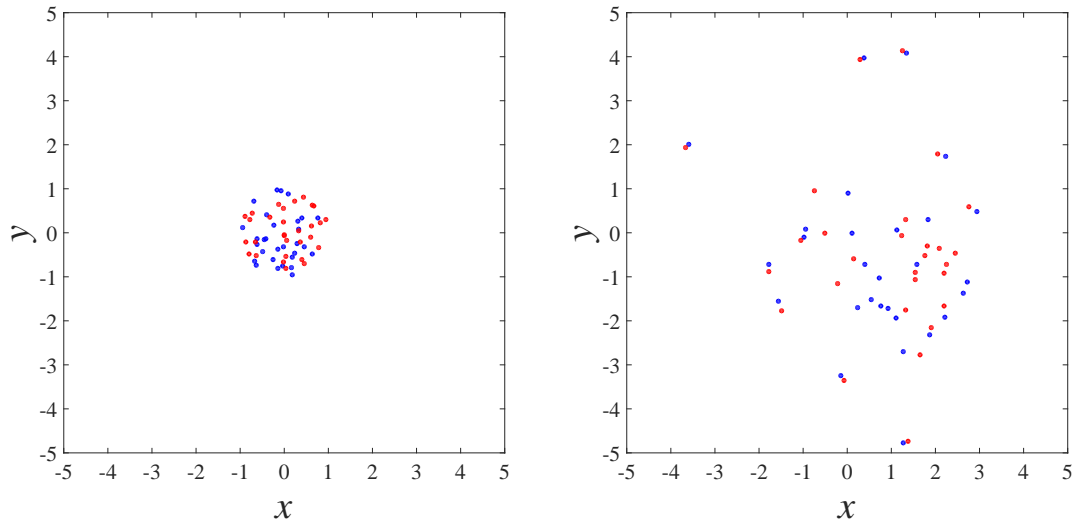


Figure 3.1: Initial positions (left) and positions after 10 time units (right) simulating the motion of 30 positive vortices (red) and 30 negative vortices (blue) in an infinite plane. Note that the vortices have spread out. The size of the markers does not correspond to some vortex core size; vortices are treated as points in our model.

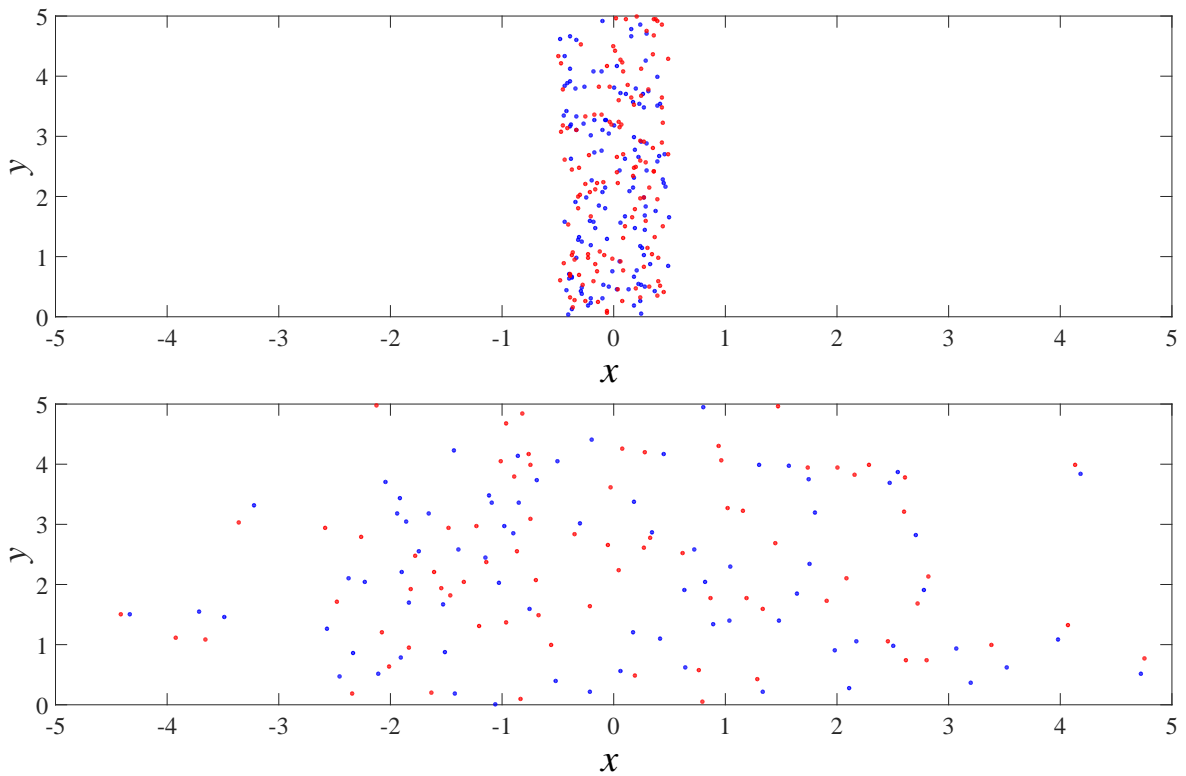


Figure 3.2: Initial vortex configuration (top) and vortex configuration after 100 time units simulating the motion of 250 vortices in a periodic domain.

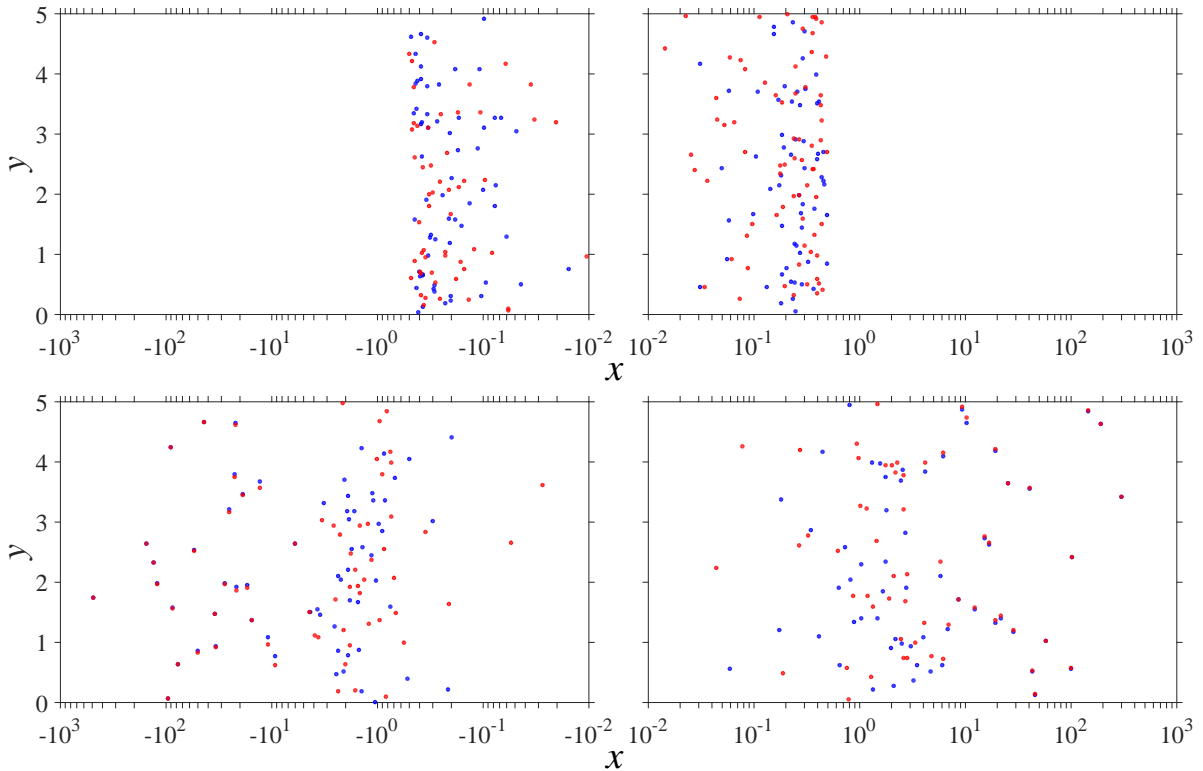


Figure 3.3: As in Fig. 3.2, but with a logarithmic scale for x to highlight the large range of positions. Initially the vortices are generated within $-0.5 \leq x \leq 0.5$; at $t = 100$ they are within $-1000 \leq x \leq 1000$.

To simulate the periodic boundary at $y = 0$, $y = 5$, we use so-called ‘ghost’ vortices: the actual domain and vortices within it are repeated several times above and below, and the positions of the vortices in these repetitions are updated to constantly match the positions of the true vortices. A schematic of this is presented in Fig. 3.4. When a vortex crosses the periodic boundary its position is instantaneously updated so as to remain within the actual domain: if T_y is the period of the domain in the y -direction, then at each time step the position of each vortex is transformed according to $(x_i, y_i) \rightarrow (x_i, y_i \pmod{T_y})$. Theoretically an infinite number of repetitions would exactly mimic a periodic domain. In practice it is reasonable to truncate after only a few repetitions, as the contribution of the vortices to the velocity is proportional to $1/r$ with r the distance between vortices.

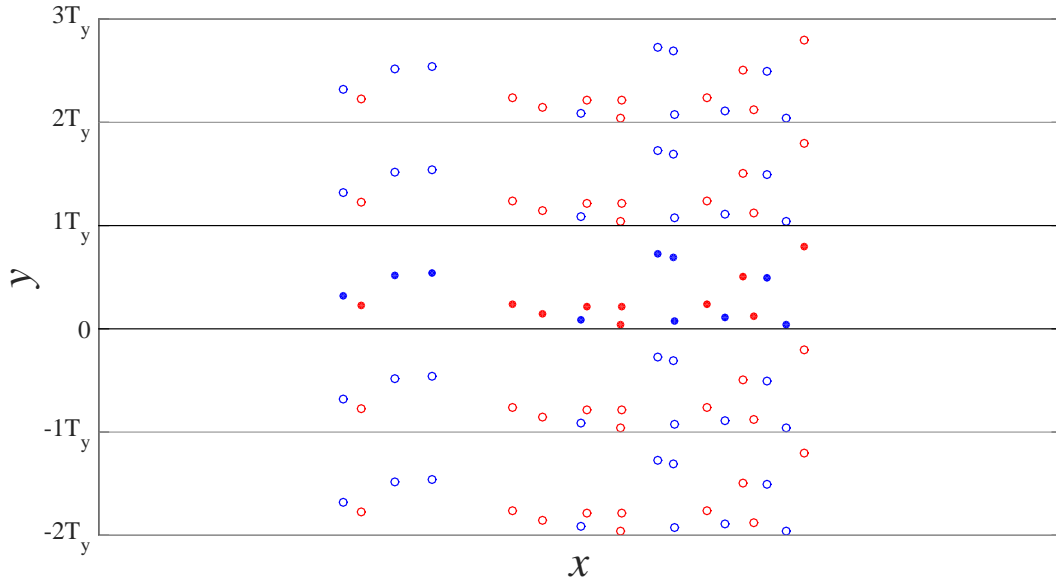


Figure 3.4: Schematic of the technique employed to simulate a domain with periodic boundaries in y . The actual system is in the strip $0 \leq y \leq T_y$; the other strips (two above and two below) contain ‘ghost’ vortices.

3.2 Runge-Kutta Methods

We use the Runge-Kutta family of time-stepping methods introduced in [17], which can be viewed as an extension of the familiar Euler method, with particular methods having a range of orders of truncation errors. The mechanism by which the methods work can be seen intuitively as a linear combination of evaluations of a given time-derivative at the current state of the system and at temporary predicted future states, with coefficients such that the combination of terms agrees with the Taylor series expansion of the function up to a truncation order. We refer to n^{th} -order Runge-Kutta methods as RKn methods.

For a function $\dot{y} = f(t, y)$, using the usual notation for temporal derivatives, the value of y at time step $n + 1$, y_{n+1} , is given by:

$$y_{n+1} = y_n + \sum_{i=1}^s hb_i k_i,$$

where h is the step size, and:

$$\begin{aligned} k_1 &= f(t_n, y_n), \\ k_2 &= f(t_n + c_2 h, y_n + ha_{21} k_1), \\ k_3 &= f(t_n + c_3 h, y_n + h(a_{31} k_1 + a_{32} k_2)), \\ &\vdots \\ k_s &= f(t_n + c_s h, y_n + h(a_{s1} k_1 + a_{s2} k_2 + \dots + a_{s,s-1} k_{s-1})). \end{aligned}$$

The particular Runge-Kutta method is specified by the number of stages $s \in \mathbb{N}_+$, and the coefficients, weights and nodes a_{ij} , b_i , $c_i \in \mathbb{R}$ respectively.

For our system of coupled ODEs $\dot{\mathbf{x}} = f_x(\mathbf{x}, \mathbf{y})$, $\dot{\mathbf{y}} = f_y(\mathbf{x}, \mathbf{y})$, which have no time-dependence, this extends to:

$$\mathbf{x}_{n+1} = \mathbf{x}_n + \sum_{i=1}^s hb_i \mathbf{k}_{xi} \qquad \mathbf{y}_{n+1} = \mathbf{y}_n + \sum_{i=1}^s hb_i \mathbf{k}_{yi}$$

$$\begin{aligned} \mathbf{k}_{x1} &= f_x(\mathbf{x}, \mathbf{y}), & \mathbf{k}_{y1} &= f_y(\mathbf{x}, \mathbf{y}), \\ \mathbf{k}_{x2} &= f_x(\mathbf{x} + ha_{21}\mathbf{k}_{x1}, \mathbf{y} + ha_{21}\mathbf{k}_{y1}), & \mathbf{k}_{y2} &= f_y(\mathbf{x} + ha_{21}\mathbf{k}_{x1}, \mathbf{y} + ha_{21}\mathbf{k}_{y1}), \\ &\text{etc.} & &\text{etc.} \end{aligned}$$

Values of s , a_{ij} , b_i , and c_i for selected methods are detailed in Appendix A. We use the 6th-order method given in this appendix for our simulations.

3.3 Tests

3.3.1 Two-Vortex Interactions

We can use the motion of two-vortex configurations given in Sec. 2.2.2 to test the quantitative accuracy of our simulation. As mentioned, a vortex-antivortex pair will translate linearly, and a pair of vortices with identical circulation will follow a circular path around their combined center. The separation of the vortices should be constant.

When we simulate these interactions we find the trajectories to be of the correct form, though the separation of vortices deviates from the initial value. For vortex-antivortex pairs simulated using the 6th-order method in Appendix A with step size $h = 10^{-2}$ the relative (with respect to their initial separation) deviation is of the order of 10^{-14} over 100 time units; smaller step sizes lead to larger values, so we are led to believe this deviation stems from floating-point errors. For the pairs with identical circulation we find a deviation of the order of 10^{-2} over 100 time units, a deviation due to the numerical method.

3.3.2 Periodic Domain

We perform the same two-vortex tests as above for a periodic domain and find similar results.

To gain a better understanding of how many repetitions of the domain are necessary to mimic a periodic domain we make use of a well known phenomena: various (in fact an infinite number of) configurations of vortices are either stationary or in relative equilibria, see e.g. [18]. One such stationary configuration is an infinite line of equally spaced vortices with alternating sense. In our periodic domain this will be a line with an even number of vortices of alternating sense, equally spaced including the distance between the vortices nearest the boundary. We use 20 vortices, spaced 0.25 distance units apart in a periodic domain with $T_y = 5$. We simulate this configuration with different numbers of repetitions (R) and record the time (t_c) it takes for any vortex to move more than 0.01 distance units, after which the configuration rapidly breaks down. For example, Fig. 3.4 shows $R = 2$ repetitions.

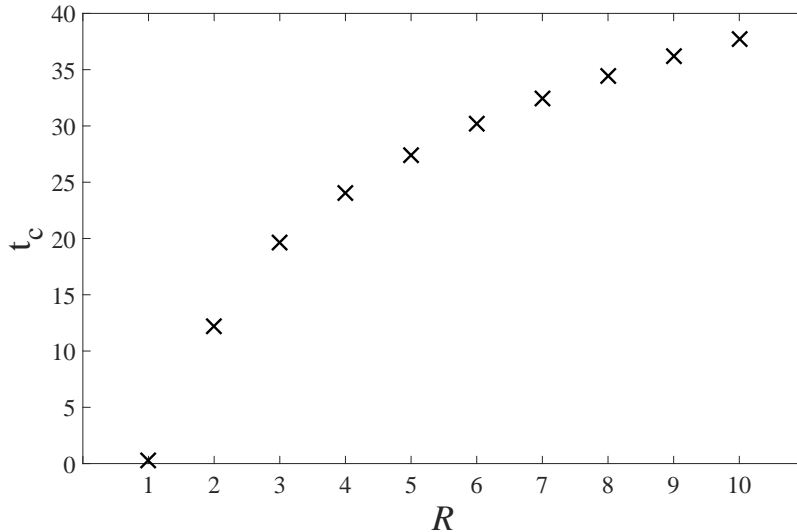


Figure 3.5: Time t_c taken for a given configuration (here a line of vortices with alternating circulation) to become unstable (defined as when any vortex drifts by 0.01 units or more from its initial position) as a function of the number of repetitions.

From Fig. 3.5, we see that the value of t_c is less than 2.5 time units better for 10 realisations than for 9, and we judge that the extra processing time needed to improve on this is not necessary as this configuration is very sensitive to perturbations, while the configurations we are working with are insensitive due to the chaotic nature of vortex motion. All further simulations of periodic domains are performed using $R = 10$.

3.4 Assessing Accuracy

3.4.1 Runge-Kutta-Fehlberg Methods

A well known subset of Runge-Kutta methods contains the Runge-Kutta-Fehlberg methods (RKF), proposed by Fehlberg in [19]. These methods use additional evaluations of the function to calculate derivatives: one evaluation used to evolve the system as with classical RK methods, and a second embedded evaluation which is of a higher order and allows an estimation of the local truncation error by complete coverage of the leading truncation error term. We refer to these methods as $RKn(m)$ methods, where n is the order of the method used to evolve the system and m is the order of the higher order embedded method. Fehlberg provides a range of such methods in references [20–22].

The most frequent use for the RKF methods is to implement an adaptive scheme, where the step size is reduced when the local truncation error is above a chosen threshold (and tentatively increased when the local truncation error is below some other threshold, for efficient integration). While the local truncation error estimates are good measures of local accuracy, we need a measure of the global accuracy of the simulations. The global truncation error for RK methods can be estimated by the order of the method and step size used, but this estimate is potentially complicated by two things here: we

are integrating a large number of coupled ODEs, not a single ODE, and if we use an adaptive scheme the step size will not be constant.

3.4.2 Autonomous Hamiltonian

The autonomous Hamiltonian for a system of n point vortices with circulations Γ_i and separations r_{ij} as in Sec. 2.2 is given by:

$$H = -\frac{1}{4\pi} \sum_{i=1}^n \sum_{j=1}^{n'} \Gamma_i \Gamma_j \ln r_{ij}, \quad (3.1)$$

as derived by Kirchhoff in [23]. This quantity, which here describes the kinetic energy of the fluid motion about the vortices as discussed in [12], is conserved, and can be easily calculated. We can use the absolute relative difference in the Hamiltonian at each time:

$$|\Delta H_R(t)| = \left| \frac{\Delta H(t)}{H(0)} \right| = \left| \frac{H(t) - H(0)}{H(0)} \right|,$$

as an objective and comparable measure of the accuracy of each realisation of our simulation. The calculation of the Hamiltonian does not add any significant processing time to our simulation, and we are able to examine both the local and global changes over time

In Fig. 3.6 we give the results of this test for the infinite domain scenario described in Sec. 3.1.1. We use the RK6 method detailed in Appendix A to evolve the system through 100 time units using a range of values for our step size h .

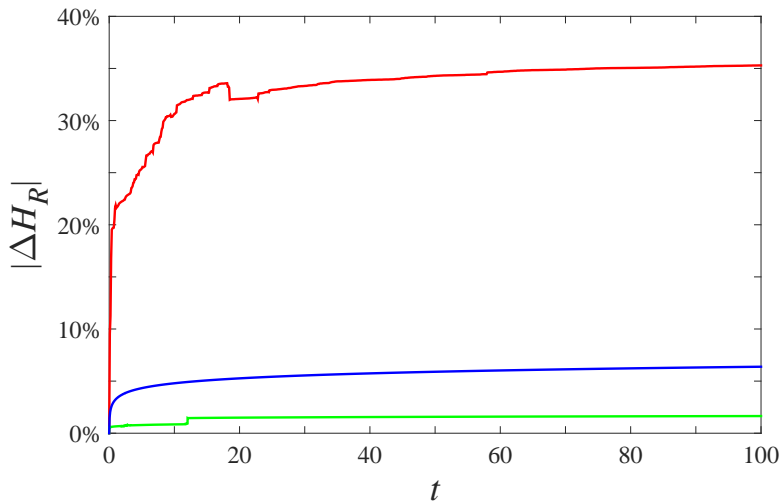


Figure 3.6: $|\Delta H_R|$ for 250 vortices with a net circulation of 0 in an infinite domain, expressed as a percentage with step size $h = 10^{-1}$ (red), $h = 10^{-2}$ (blue), and $h = 10^{-3}$ (green)

In a periodic domain the autonomous Hamiltonian takes a slightly different form:

$$H = -\frac{1}{4\pi} \sum_{i=1}^n \sum_{j=1}^{n'} \Gamma_i \Gamma_j \ln r_{ij} - \frac{1}{4\pi} \sum_{k=1}^R \sum_{i=1}^n \sum_{j=1}^n \Gamma_i \Gamma_j \ln r_{ij}^k, \quad (3.2)$$

where R is the number of repetitions we use to mimic a periodic domain, and r_{ij}^k refers to the distance between the i^{th} vortex in the actual domain and the j^{th} vortex in the k^{th} repetition of the domain. Note that the second term does not omit the term with $i = j$. We test the absolute relative difference as before, using a domain which has a period of 5 distance units in y , with vortices randomly placed within a strip of width 1 distance unit. $|\Delta H_R|$ calculated in this way is shown in Fig. 3.7.

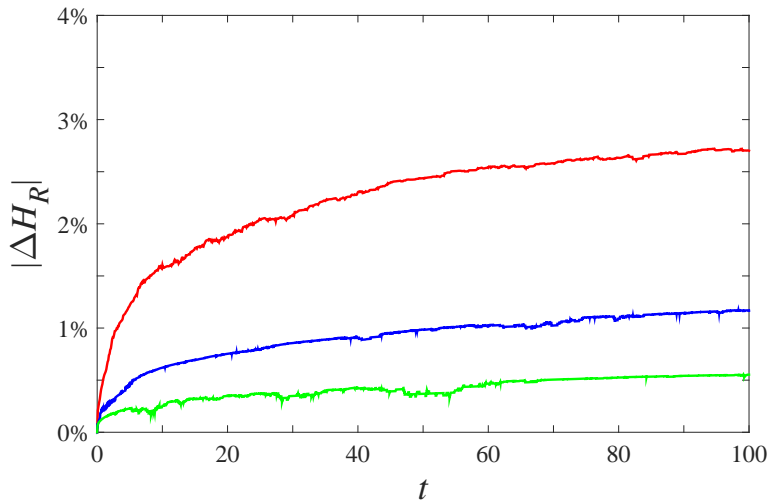


Figure 3.7: As in Figure 3.6 but for simulations in a periodic domain. Note the different scale of the y -axis.

In both cases $|\Delta H_R|$ decreases as the value of the step size h decreases, indicating a more accurate simulation. If we compare visualisations of simulations using $h = 10^{-2}$ and $h = 10^{-3}$ we see little difference. We are content to work with $|\Delta H_R| \simeq 1\%$ (so select $h = 10^{-2}$); clearly there is scope to improve upon this for future publication if desired, particularly with investigation into the efficiency in terms of the number of function evaluations required to attain a particular level of conservation of the Hamiltonian for a range of RK methods and values of h .

In the periodic domain setup the conservation of the Hamiltonian is an order of magnitude better than in the infinite domain setup. Some proportion of this may be attributed to the difference in the area in which vortices are initially placed, as when we alter the width of the strip in the periodic domain so that the initial density of vortices matches the initial density of vortices in the infinite domain, we find that the conservation of the Hamiltonian is worse, as shown in Fig. 3.8. However, this does not account for all of the difference; investigation into why this should be the case is beyond the scope of this work.

We return to the modifications to the PVM described in Sec. 2.2.2. If pairs of vortices are suddenly removed from the model (so as to encapsulate annihilations), the value of the Hamiltonian will change, and distinguishing the effects of this from the

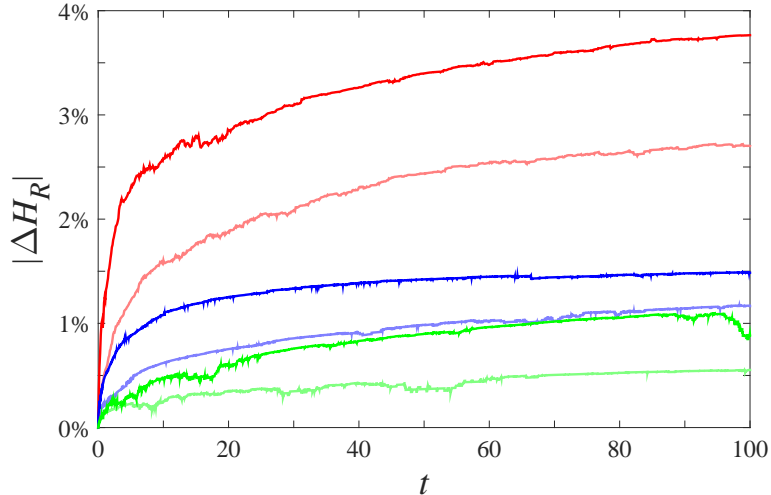


Figure 3.8: $|\Delta H_R|$ from Fig. 3.7 (light lines), and $|\Delta H_R|$ with altered initial number density of vortices (dark lines)

effects of our numerical method on $|\Delta H_R|$ is not trivial. This breaks the Hamiltonian description of our system.

Similarly, the motion about Rankine vortices does not precisely match that defined by the Hamiltonian of the system, though the effects on $|\Delta H_R|$ may be more subtle here and so harder to distinguish. A Rankine velocity profile should not be necessary with a suitable time-stepping technique and step size; for the sake of ease when interpreting $|\Delta H_R|$, we make neither modification.

Finally, in Table 2.1 we present some summary statistics concerning the values of $|\Delta H_R|$ at the final time step in the simulations our main results are based upon.

Min	Max	Mean	Standard Deviation	Q_1	Q_2	Q_3
0.0107	0.0261	0.0151	0.00252	0.0134	0.0146	0.0167

Table 3.1: Summary statistics (to 3.S.F.) of the values for $|\Delta H_R|$ from 400 realisations of our key simulation. Q_1 , Q_2 and Q_3 denote the first, second and third quartiles.

3.5 Identifying Vortex Dipoles

Two separate processes lead to the spread of vortices in our model: the vortex-antivortex pairs which move rapidly away for the main group, and the diffusion of the main group. The first effect is perhaps more surprising, and we touch upon this in our conclusions. The example in Fig. 3.9 shows clearly the trajectories of vortex pairs which have escaped from the main group.

We are interested in the diffusion of the main group, and as the identification of dipoles by eye would be impractical and subjective we developed an algorithm to distinguish them from the main group. At each time step we establish a measure β of the similarity in velocity:

$$\beta_{ij} = \sqrt{\left(\frac{u_{ix} - u_{jx}}{u_{ix}}\right)^2 + \left(\frac{u_{iy} - u_{jy}}{u_{iy}}\right)^2},$$

with u_{ix} the x -component of the i^{th} vortex's velocity and so on. It should be apparent that $\beta_{ij} \rightarrow 0$ as the velocities approach being identical, and that $\beta_{ij} \neq \beta_{ji}$ in general. If β_{ij} and β_{ji} are both less than some threshold β_C , then we consider the ratio γ_{ij} of the separation of the pair and their separation from the nearest other vortex. If γ_{ij} is below some critical value γ_C we identify the pair as an escaping dipole.

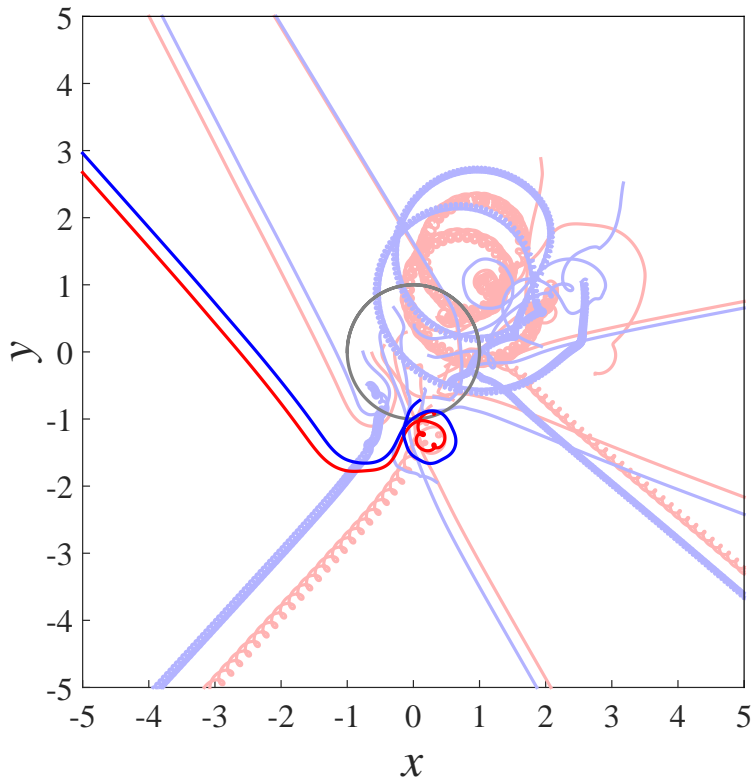


Figure 3.9: The trajectories of 15 vortices with positive circulation (red) and 15 vortices with negative circulation (blue) over 20 time units in an infinite domain. The initial configuration was within the grey circle (a visual marker, not a physical object in the simulation). The trajectories of the vortices forming one dipole are highlighted in bold; other such dipoles are evident. A similar image is given on the cover of this report.

After experimenting a little, we use $\beta_C = 1/10$ and $\gamma_C = 1/3$, although a range of values give almost identical results. We give an example of the pairs this technique identifies in Fig. 3.10.

We found this method far more likely to fail to identify a dipole than to incorrectly identify two vortices as a pair. The majority of these failures occurred when two dipoles move away from the main group, pass close enough to each other to fail the separation test, before being reidentified at a later time. To account for this we examine the data on pairing: if two vortices are identified as a dipole, then not identified for

up to 5 time units, then reidentified, we identify them as a dipole during that gap post hoc. Observing visualisations of the simulation with dipoles identified verifies this technique.

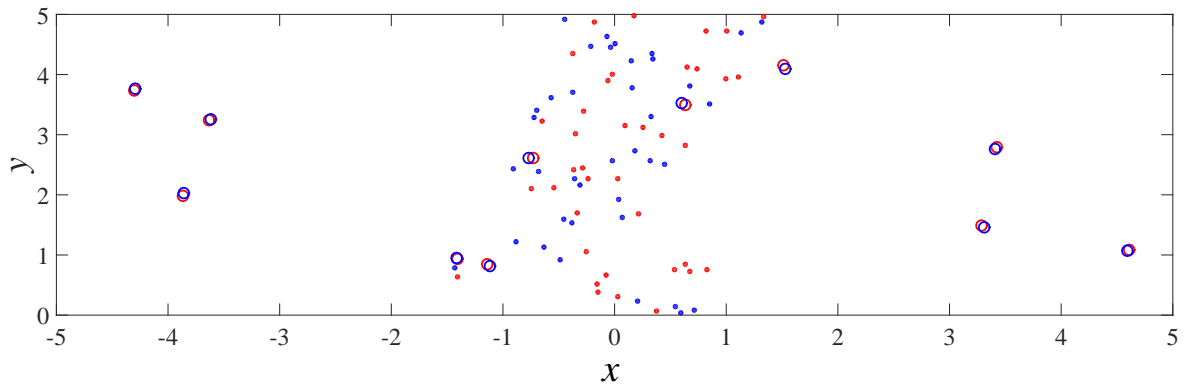


Figure 3.10: Demonstration of our technique. Vortex dipoles (hollow circles) have been automatically identified. We refer to the remaining vortices (solid circles) as the main group. Dipoles with a small separation between the constituent vortices may appear as a single marker, but do consist of two vortices.

Chapter 4

Anomalous Diffusion

4.1 Standard Diffusion

Before discussing anomalous diffusion we illustrate a standard diffusion process, in order to have something to contrast anomalous diffusion with.

4.1.1 The Diffusion Equation & Gaussian Solution in One Dimension

Consider the diffusion equation in one spatial dimension: $u_t = Du_{xx}$, where $u(x, t)$ is a density as a function of position and time, D is the constant diffusion coefficient, and subscripts denote partial derivatives. We now proceed to derive a Gaussian solution to this one-dimensional diffusion equation. Using the convention:

$$\hat{f}(k, t) = \mathcal{F}[f(x, t)] = \int_{-\infty}^{\infty} f(x, t) e^{-ikx} dx,$$
$$f(x, t) = \mathcal{F}^{-1}[\hat{f}(k, t)] = \frac{1}{2\pi} \int_{-\infty}^{\infty} \hat{f}(k, t) e^{ikx} dk,$$

for the Fourier transform, we take the Fourier transform of u : let $\hat{u} = \hat{u}(k, t) = \mathcal{F}_x[u(x, t)]$, then $u_t = \hat{u}_t$, $u_{xx} = -k^2 \hat{u}$. We restate the diffusion equation as:

$$\hat{u}_t = -Dk^2 \hat{u}.$$

It is trivial to show that $\hat{u} = B \exp\{-Dk^2 t\}$ for some constant B determined by initial conditions. We use the inverse Fourier transform (IFT) and a standard result:

$$\mathcal{F}^{-1} \left[\sqrt{\frac{\pi}{a}} \exp \left\{ \frac{-k^2}{4a} \right\} \right] = \exp \{-ax^2\},$$

and take the IFT of our solution for \hat{u} :

$$u(x, t) = B \sqrt{\frac{1}{4Dt\pi}} \exp \left\{ -\frac{x^2}{4Dt} \right\}, \quad (4.1)$$

a Gaussian solution where B is a constant to be determined from initial conditions and $\sqrt{1/4Dt\pi}$ is a scaling factor that keeps the area under the curve constant. A Gaussian function has the form:

$$f(x) = a \exp \left\{ -\frac{(x - b)^2}{2\sigma^2} \right\},$$

a symmetric ‘bell’ curve centered about b , with the width defined by σ^2 , and a a scaling parameter. Comparing this to our solution (4.1) of the diffusion equation, it is evident that $\sigma^2 \propto t$ for a normal diffusion process.

4.1.2 Random Walk Process

The use of random walk processes to model diffusion processes, such as Brownian motion, is well established, see e.g. [24]. We use such a process to illustrate a standard diffusion process and the linear change in variance of a fitted Gaussian over time. We simulate a random walk process by generating 250,000 non-interacting ‘particles’ in a vertical strip from $x = -0.5$ to $x = 0.5$ and moving each particle a fixed distance in a random direction at each time step, recording the x -positions of the particles at each time. We use a domain which is periodic in y for consistency with our vortex simulations, although the results are identical in a non-periodic domain. Some example trajectories are shown in Fig. 4.1.

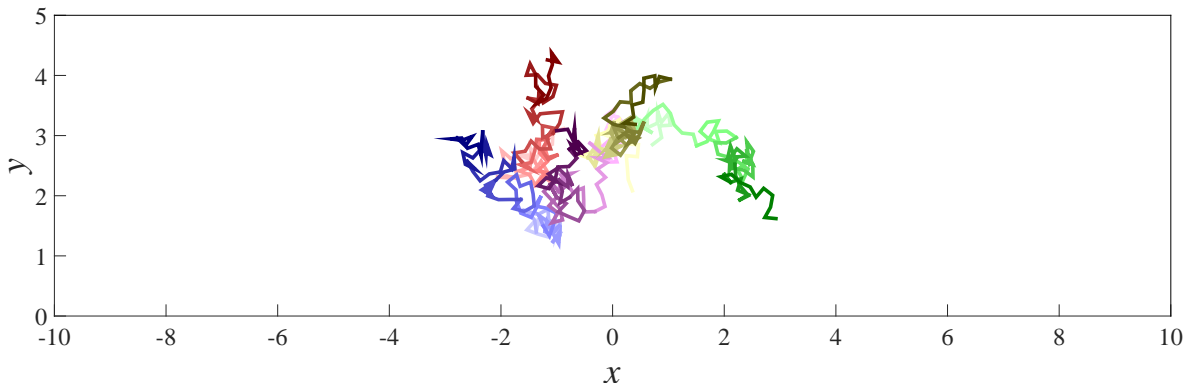


Figure 4.1: Sample trajectories of 5 ‘particles’ following random walks for 100 time steps. Particles have higher speeds here than in our simulated random walk, to exaggerate their trajectories for this figure.

We count the number of particles in each region of width 0.1 in x , normalise the frequency, and make use of Matlab’s in-built function *fminsearch* [25] to fit a Gaussian function, as shown in Fig. 4.2. Although we start with a square distribution of particles, the distribution rapidly tends to a Gaussian form centred about $x = 0$. We plot the value of σ^2 for the fitted Gaussian against time in Fig. 4.3.

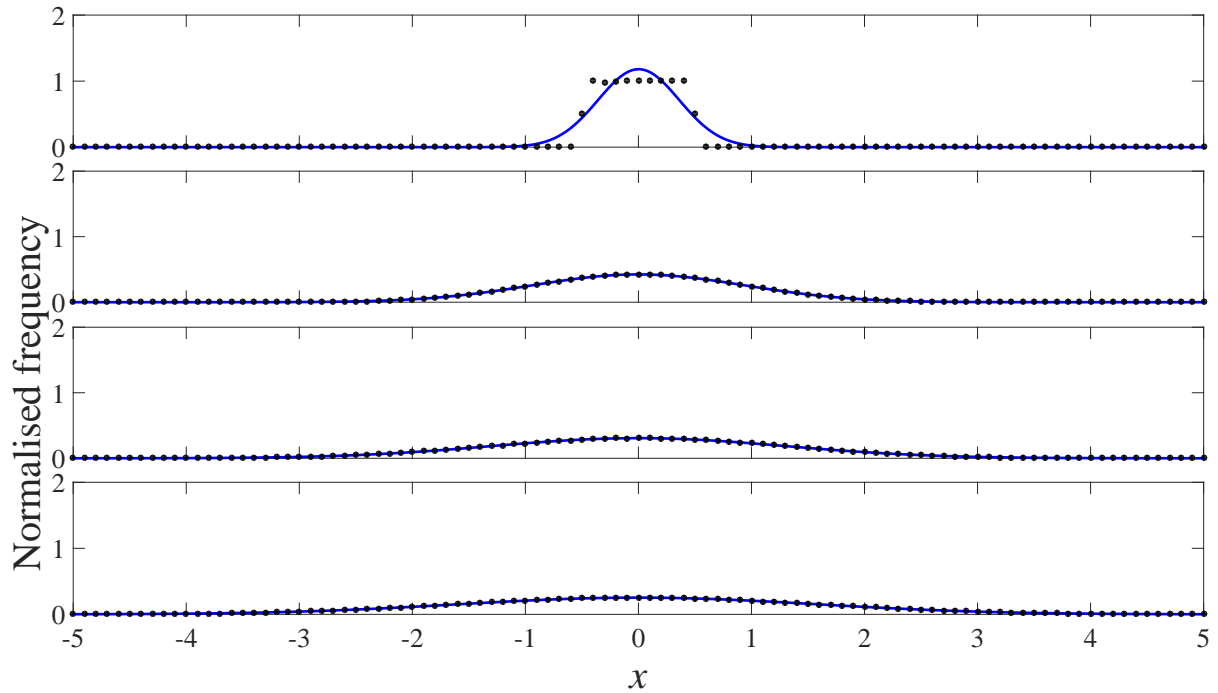


Figure 4.2: x -distribution (black dots) of ‘particles’ in our random walk process at the start ($t = 0$) of the simulation (top) and at three later times ($t = 10$, $t = 20$, $t = 30$), with Gaussian functions (blue) fitted to the distributions.

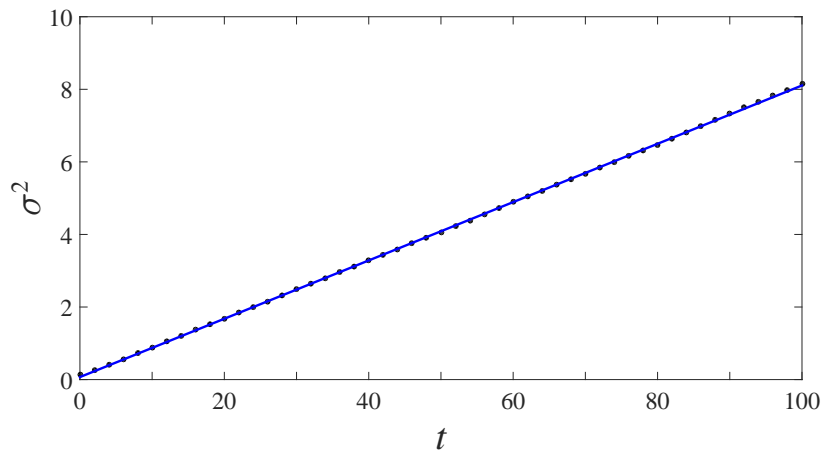


Figure 4.3: σ^2 (black dots) of the Gaussian function fitted to the x -distribution of ‘particles’ in the random walk process, with fitted line (blue). Note that σ^2 is proportional to t , as expected.

This illustrates the linear relationship between σ^2 and t in a standard diffusion process. From our solution (4.1) to the diffusion equation, we have $\sigma^2 = 2Dt$, so we can recover a value for D . In this example we find $D = 0.0402$ (*3S.F.*), which is within 0.5% of the speed we gave to the particles.

4.2 Subdiffusion & Superdiffusion

We now return to the one-dimensional diffusion equation and consider a more general diffusion coefficient: $D = D_0 t^\alpha$ for some constants D_0 and α , so that the rate of diffusion varies with time. Setting $\alpha = 0$ recovers standard diffusion. Setting $\alpha < 0$ implies that the rate of diffusion diminishes in time, while setting $\alpha > 0$ implies that the rate of diffusion increases in time; the latter two situations are respectively referred to as subdiffusion and superdiffusion, both forms of anomalous diffusion.

We begin by performing dimensional analysis on the generalised diffusion coefficient. For consistency we must have $[u_t] = [D][u_{xx}]$. In this context u is a number density, so has dimensions of $1/L$ in 1D. Then:

$$\frac{1}{LT} = [D] \frac{1}{L^3} \implies [D] = \frac{L^2}{T}.$$

We must have $[D_0] = L^2/T$ to be dimensionally consistent in the standard diffusion case $\alpha = 0$. This implies that $[D] = L^2/T^{1-\alpha}$, so we introduce a constant t_0 with $[t_0] = T$, and use:

$$D = D_0 \frac{t^\alpha}{t_0^\alpha}, \quad (4.2)$$

which is dimensionally consistent. We transform to the frequency domain:

$$\begin{aligned} \hat{u}_t &= -D_0 \frac{t^\alpha}{t_0^\alpha} k^2 \hat{u} \\ \implies \hat{u} &= B \exp \left\{ -\frac{D_0 t^{\alpha+1} k^2}{(\alpha+1)t_0^\alpha} \right\}, \end{aligned}$$

which we can rewrite as:

$$\hat{u} = B \sqrt{\frac{t_0^\alpha (\alpha+1)}{4\pi D_0 t^{\alpha+1}}} \sqrt{\frac{4\pi D_0 t^{\alpha+1}}{t_0^\alpha (\alpha+1)}} \exp \left\{ -\frac{D_0 t^{\alpha+1} k^2}{(\alpha+1)t_0^\alpha} \right\}.$$

Using the same IFT result as in Sec. 4.1.1, we find:

$$u(x, t) = B \sqrt{\frac{t_0^\alpha (\alpha+1)}{4\pi D_0 t^{\alpha+1}}} \exp \left\{ -\frac{t_0^\alpha (\alpha+1) x^2}{4D_0 t^{\alpha+1}} \right\},$$

and inspection of dimensions confirms that this is a number density. Comparing to the Gaussian function, we find $\sigma^2 \propto t^{\alpha+1}$, which is consistent with the result for standard diffusion in Sec. 4.1. As $\alpha < 0$ implies subdiffusion and $\alpha > 0$ implies superdiffusion, we visualise the characteristic relationships between σ^2 and time for the three categories of diffusion considered here in Fig. 4.4.

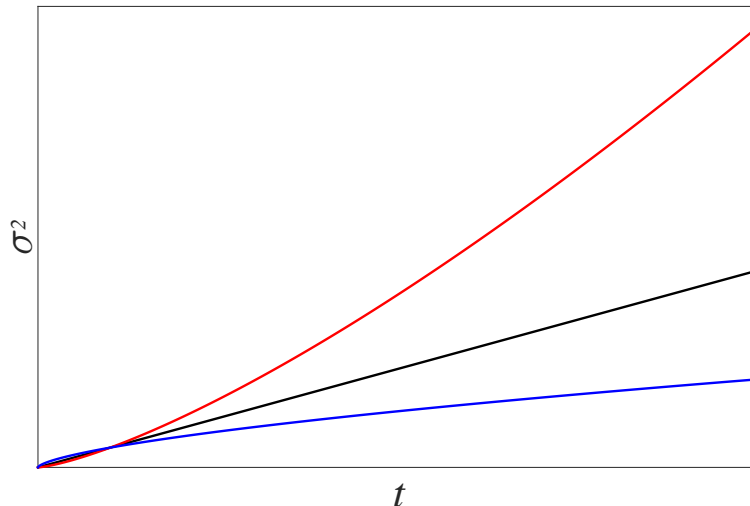


Figure 4.4: Diagram showing how the variance σ^2 of Gaussian distributions following subdiffusion (blue), diffusion (black), and superdiffusion (red) changes in time.

4.3 Diffusion of Point Vortices with Unit Circulation

We place 250 vortices, half with positive circulation and half with negative circulation, randomly in a strip from $x = -0.5$ to $x = 0.5$ in a domain which is periodic in y , with the period of the domain $T_y = 5$ and 10 repetitions of the domain above and below to simulate this periodicity. We use the RK6 method detailed in Appendix A, a step size of 10^{-2} time units, and allow the simulation to run for 100 time units. We record the positions of the vortices at each time step, from which we can infer their velocities and the pairing of vortices, and explore the statistics of their dynamics.

4.3.1 Overall Dynamics

The vortices are seen to spread out from the initial strip in two key fashions: vortex dipoles form and move rapidly away from the main group, and the main group is seen to spread out, generally in an inhomogeneous manner within an individual realisation. We sort the x -positions of the vortices into bins of width 0.1 and normalise the frequency. From a cursory inspection of Fig. 4.5 it appears that the distribution tends to a Gaussian form after some initial time, as for the random walk ‘particles’ in Fig. 4.2.

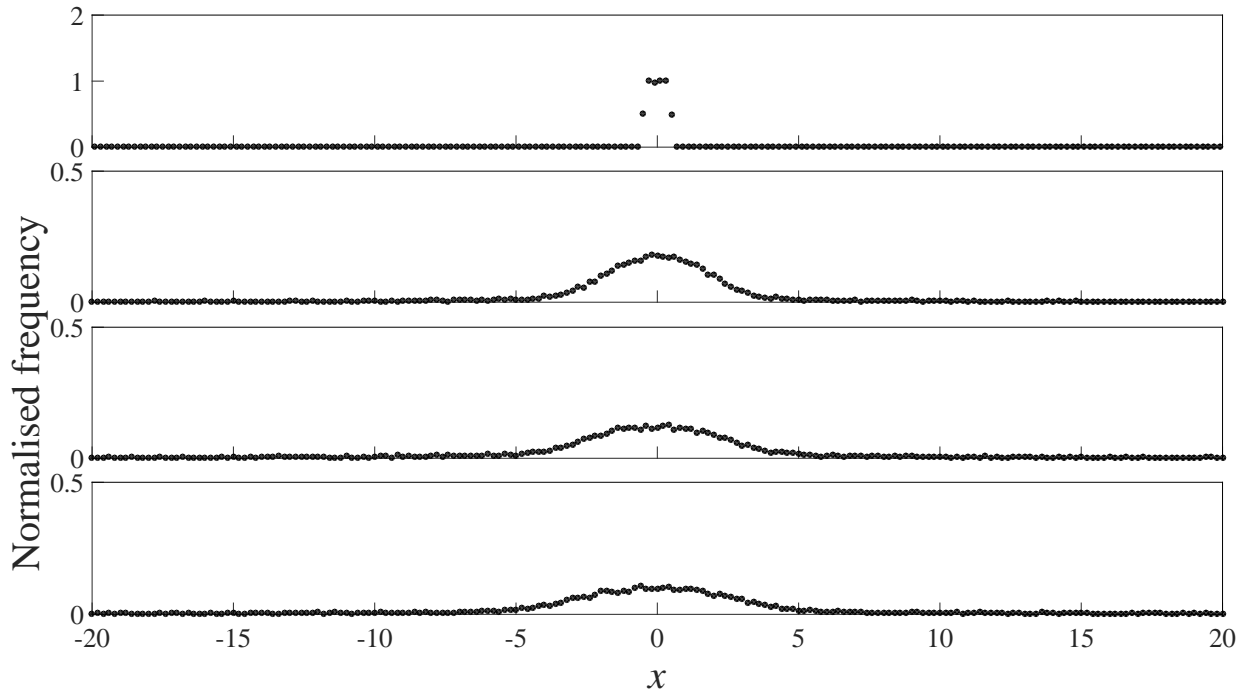


Figure 4.5: Normalised x -distribution of vortices: (top to bottom) initially, after 30 time units, after 60 time units, and after 90 time units. Note the changed y -scale on the latter 3 plots. The area under the curve may not appear to be conserved at first glance, but vortices are present at a low frequency to values of x far outside the range shown.

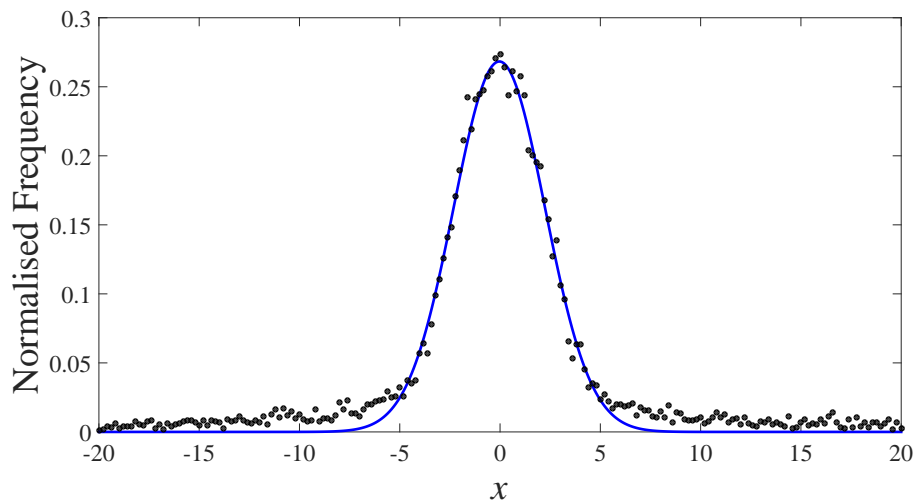


Figure 4.6: Detail of the x -distribution of vortices after 90 time units (black dots) with a fitted Gaussian function in blue.

On closer inspection it becomes apparent that a Gaussian may not be the most appropriate function to fit. In Fig. 4.6, the Gaussian appears to fit the central region

of the distribution reasonably well. However, the Gaussian function tends to zero while the distribution is still clearly non-zero, and the distribution of vortices far away from the line $x = 0$ skews the variance of the Gaussian. We find this fit unsatisfactory; visually the fitted curve does not match the data, and when we calculate the sum of square errors (SSE) we find a value on the order of 10^1 , compared to a typical SSE of 10^{-1} for the Gaussian functions fitted to the random walk data in Sec. 4.1.2.

Experimenting with various functional forms does not yield a satisfactory fit without involving additional parameters or somewhat unusual functional forms, and as John von Neumann (supposedly) had it: “With four parameters I can fit an elephant, and with five I can make him wiggle his trunk.” - adding additional parameters with no justification may give a pleasing fit, but the fit has a level of arbitrariness to it, and is more likely to obfuscate the underlying processes than to allow any insight.

To make progress in analysing the spread and diffusion of vortices, we separate the vortices into paired and unpaired vortices using the technique described in Sec. 3.5. We examine the proportion, across all 400 realisations, of vortices identified as pairs in Fig. 4.7.

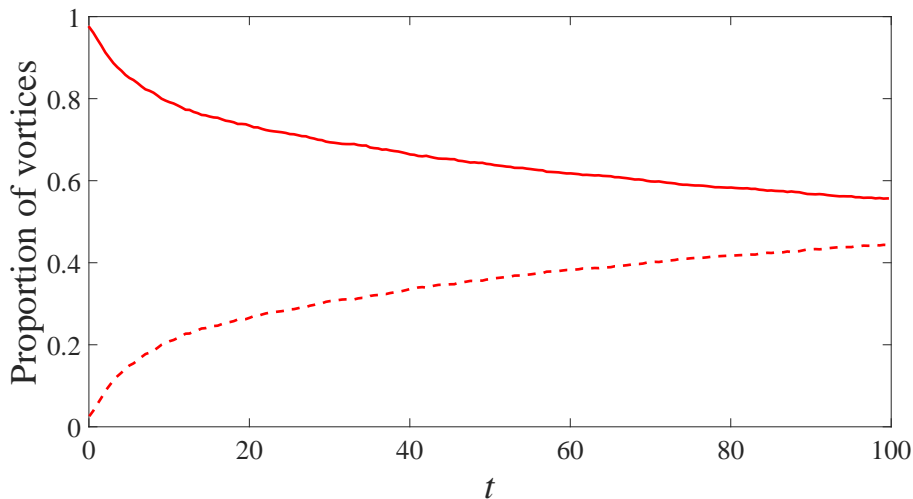


Figure 4.7: Proportion of vortices identified as pairs (dashed line) and proportion not identified as pairs (solid line) by our algorithm.

From Fig. 4.7, we conclude that we are not left with a deficiency of data on either the dipoles or the main group when we separate them. The rate at which pairs form is higher at earlier times; this may be related to the average separation of vortices. At earlier times the vortices are less separated, so pairs with smaller separation and thus greater speed are more likely to form than at later times. At later times pairs may not have sufficient speed to escape the main group before the chaotic flow around them disrupts the pair.

4.3.2 Dynamics of the Main Group

As with the ‘particles’ in the random walk, we can compare the distribution of vortices in our simulation to the form of the function we found for the non-standard

diffusion equation. By inspecting Fig. 4.8, we can confirm visually that a Gaussian is an appropriate function to fit to the distribution of vortices which we identify with our main group. When we calculate the SSE for this fit we find values similar to those found for Gaussian functions fitted to the random walk data, substantiating our assessment of how well a Gaussian function fits the data.

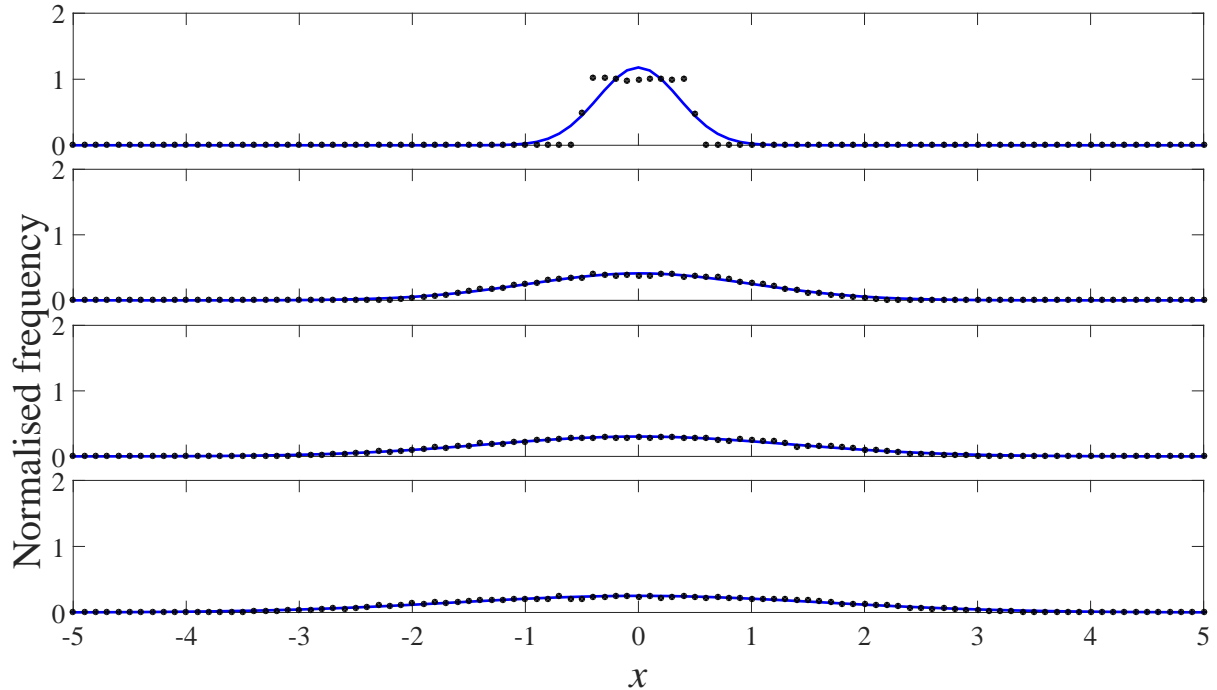


Figure 4.8: The distribution of point vortices in the main groups (black dots) with fitted Gaussian in blue. We again start with a square distribution, at $t = 0$ (top), which rapidly tends to a Gaussian distribution. Plots show the distribution (from top to bottom) at $t = 0$, $t = 10$, $t = 20$, $t = 30$.

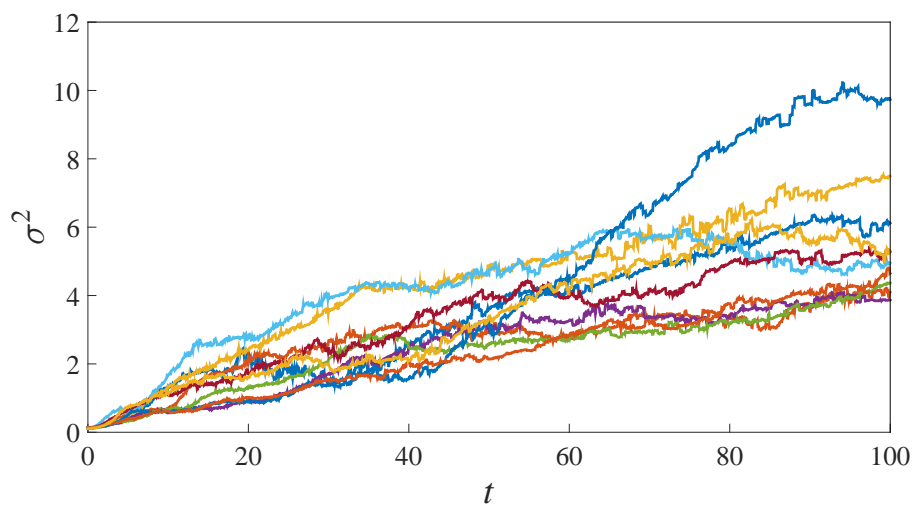


Figure 4.9: Variance (σ^2) of the Gaussian functions fitted to the x -distributions of the main cluster of vortices in 10 realisations.

We then fit Gaussian functions to the distribution of the main group over time separately for our 400 realisations and record the variance of the fitted Gaussian at each time step. The variance of the fitted Gaussian versus time is shown in Fig. 4.9 for 10 difference realisations (the initial configuration varies randomly between realisations).

Although the trajectories shown in Fig. 4.9 are not identical, they exhibit similar general behaviour. We are interested in the general diffusive behaviour of point vortices, so we take the average value, over all realisations, of σ^2 at each time step to minimise any residual transient effects due to the particular configuration of individual realisations. We refer to this sample mean vector as $\boldsymbol{\mu}$, not to be confused with the unknown population mean vector. We also calculate the sample standard deviation ($\boldsymbol{\varsigma}$) vector of σ^2 at all time steps to give an estimate of the margin of error, shown in Fig. 4.10.

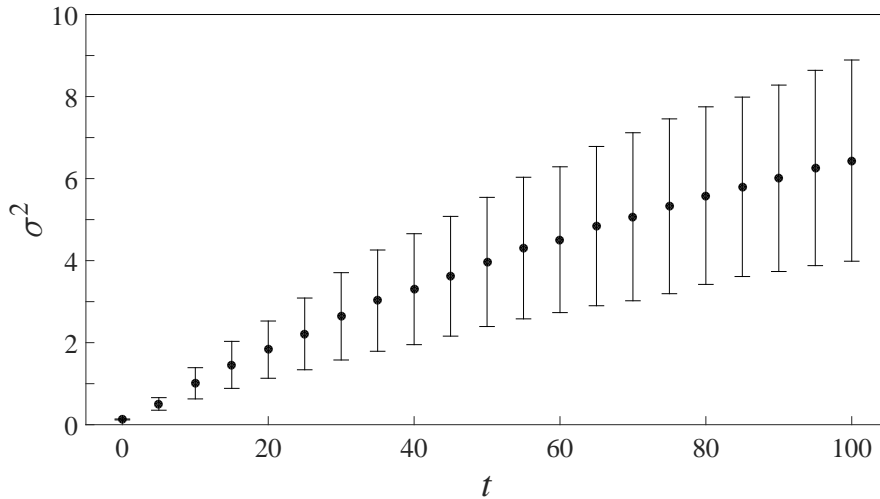


Figure 4.10: Mean variance of fitted Gaussians for 400 realisations and error bars showing $\pm 1\boldsymbol{\varsigma}$. Note that for visualisation purposes we are not displaying the full resolution of our data here.

Comparing Fig. 4.10 to the diagram shown in Fig. 4.4, it is clear that the main group of vortices follow a subdiffusion process. Recall that in our solution to the non-standard diffusion equation in Sec. 4.2 we had:

$$u(x, t) = B \sqrt{\frac{t_0^\alpha (\alpha + 1)}{4\pi D_0 t^{\alpha+1}}} \exp \left\{ -\frac{t_0^\alpha (\alpha + 1) x^2}{4D_0 t^{\alpha+1}} \right\}.$$

Comparing this to the general Gaussian function we fit to the data:

$$f(x) = a \exp \left\{ -\frac{(x - b)^2}{2\sigma^2} \right\},$$

implies that:

$$\sigma^2(t) = \frac{2D_0 t^{\alpha+1}}{(\alpha + 1)t_0^\alpha}.$$

We disregard the parameter b in the Gaussian, as it simply shifts the distribution in x ; the data is centred about 0 anyway. We establish the exponent α introduced in Sec. 4.2 by fitting a function of this form with parameters D_0 , t_0 and α to $\boldsymbol{\mu}$. We also fit to $\boldsymbol{\mu} \pm \boldsymbol{\varsigma}$ in Fig. 4.11.

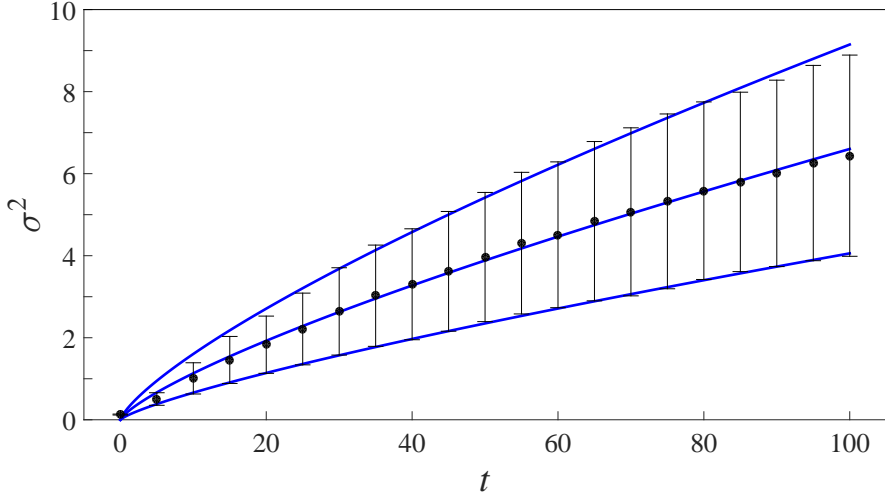


Figure 4.11: Curves fitted to the full data, plotted with the error bars shown in Fig. 4.10

From Table 4.1, the main group of vortices follow a subdiffusion process, with a value for α in the region of $(-0.2405, -0.2111)$. We give an interpretation of the parameters D_0 and t_0 in Sec. 4.4.

	α	D_0	t_0
$\boldsymbol{\mu} + \boldsymbol{\varsigma}$	-0.2405	0.0933	1.6547
$\boldsymbol{\mu}$	-0.2318	0.0688	1.3500
$\boldsymbol{\mu} - \boldsymbol{\varsigma}$	-0.2111	0.0461	0.6686

Table 4.1: Values found for the parameters α , D_0 and t_0 from fitting a function of the form $f(t) = \frac{2D_0 t^{\alpha+1}}{(\alpha+1)t_0^\alpha}$ to $\boldsymbol{\mu}$ and $\boldsymbol{\mu} \pm \boldsymbol{\varsigma}$.

There is an intuitive explanation as to why vortices should follow a subdiffusion process. The motion of a vortex in a fluid is driven by other vortices; a lone vortex is stationary. As the vortices diffuse the mean separation of the vortices increases, and so the mean speed of the vortices decreases, slowing down the diffusion process. We anticipate that as $t \rightarrow \infty$, $\langle |\mathbf{u}| \rangle \rightarrow 0$, $\langle r \rangle \rightarrow \infty$.

4.3.3 Dynamics of Escaping Dipoles

Our focus is primarily the spread of the main group of vortices, but we briefly investigate the distribution of the escaping dipoles. We show the normalised distribution of vortices in escaping pairs at one point in time in Fig. 4.12.

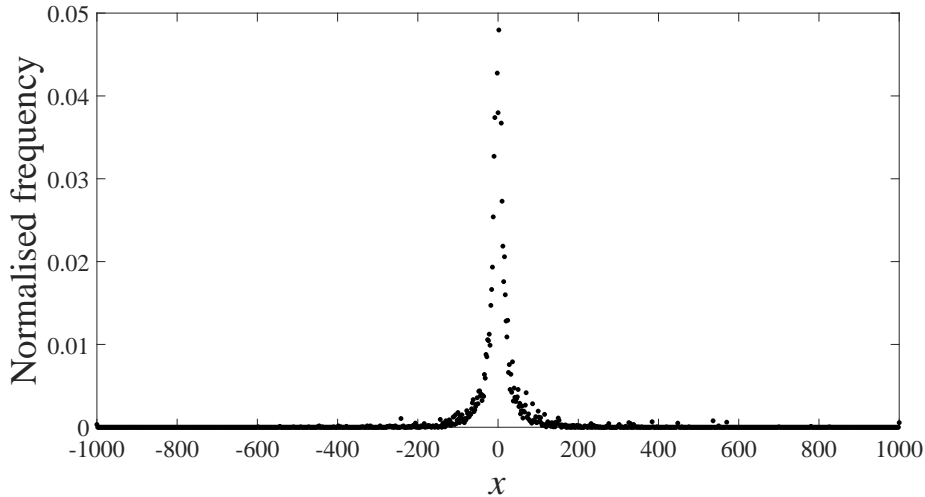


Figure 4.12: Normalised x -distribution of vortices in escaping pairs after 50 time units. Note the symmetry of the distribution.

The data shown in Fig. 4.12 appear to follow some sort of power law. We make use of the symmetry in x and plot the absolute distribution in x on a logarithmic scale in Fig. 4.13.

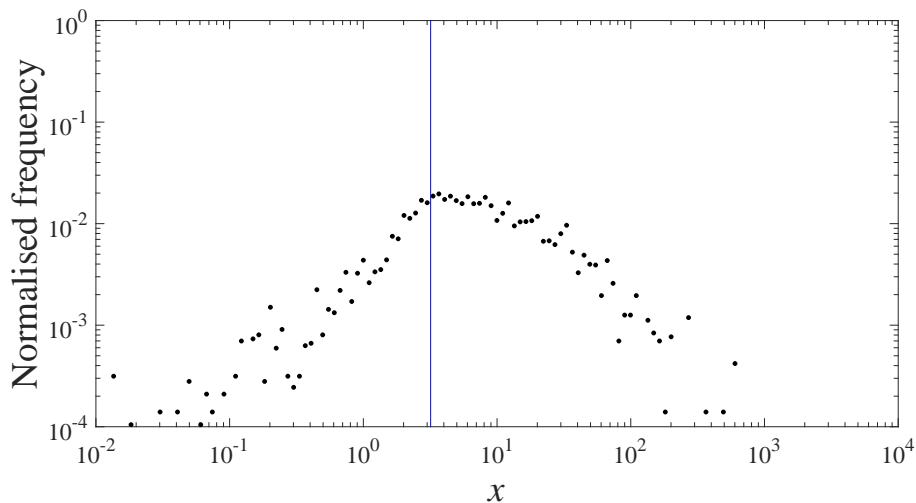


Figure 4.13: As in Fig. 4.12, but with absolute values of x and plotted on scales which are logarithmic in x and y . The blue line corresponds to the half width at tenth maximum of the Gaussian function fitted, as in Fig. 4.8, to the x -distribution of the main group at this point in time.

We also indicate the half width at tenth maximum (HWTM) of the Gaussian fitted to the x -distribution of the main group at the same point in time in Fig. 4.8. The HWTM of a Gaussian function can be calculated as $\sqrt{2 \ln 10} \sigma$, and we use it here to

give a rough indication of where the region containing the main group extends to. In Fig. 4.13 we see two different relations: in the region to the left of the HWTM the density of dipoles increases with x , and to the right the density of dipoles decreases with x . We can think of these regions as corresponding to the formation of dipoles within the main group and escaped dipoles outside the main group respectively.

If two variables have a power law relationship, the logarithms of the variables will follow a linear relationship. While there may be some evidence of this in some regions of Fig. 4.13 (such as $\text{HWTM} \leq x \leq 70$), it is unlikely that the distribution in the escaping dipole region can be fitted by a single line. The minimal data in some regions (many data points come from only ~ 10 observed vortices, or half that many dipoles, over all 400 simulations) is not conducive to fitting, and we do not attempt to quantify any potential power law at this point.

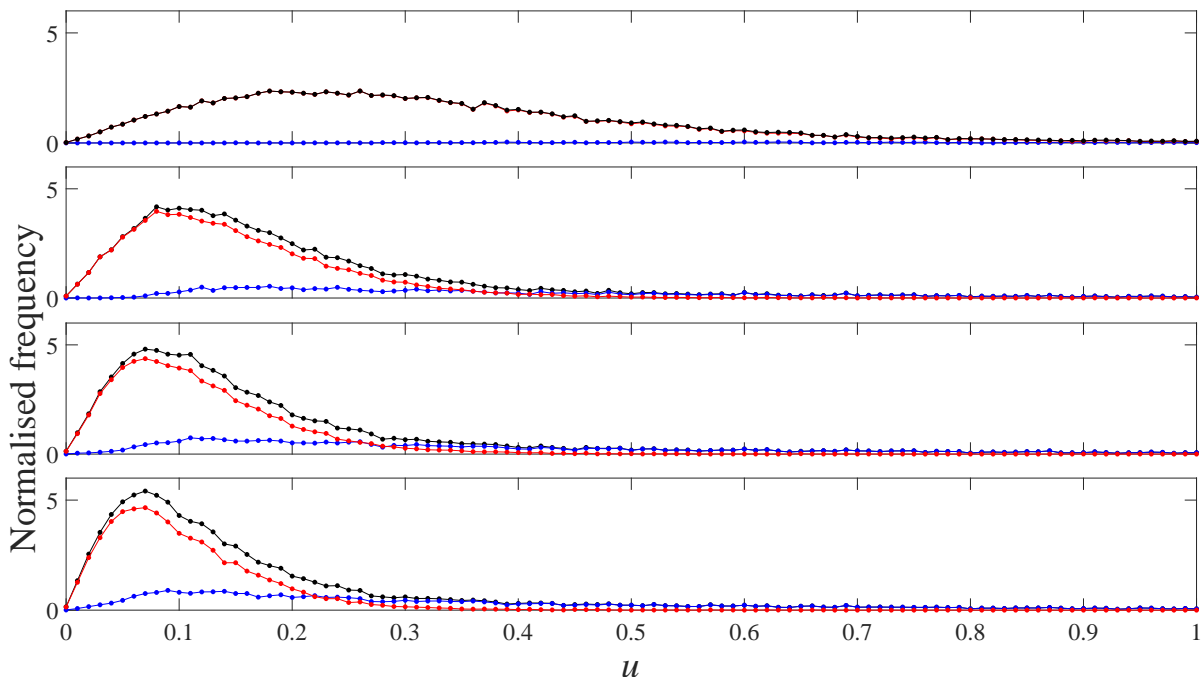


Figure 4.14: Distribution of the speed u of vortices at $t = 0$ (top), $t = 20$, $t = 40$, and $t = 60$. The overall distribution is normalised and shown in black, the distribution for vortices in the main group is shown in red, and the distribution for vortices in escaping pairs in blue. The distributions for vortices in the main group and vortices in escaping pairs are scaled so as to sum to the overall distribution.

In Fig. 4.14 we show the distribution of the speed of vortices. There are interesting parallels with the Maxwell-Boltzmann distribution for particle speeds in ideal gases. As time increases, the overall curve becomes less ‘spread out’, the height of the curve increases, and the peak moves toward the origin. For a Maxwell-Boltzmann distribution this would reflect the cooling of an ideal gas; however here we are considering vortices, not particles, in an ultracold medium. The high- u end of the distribution is dominated by escaping pairs, as seen in the bottom plot of Fig. 4.14; this may be analogous to the evaporation of the particles with greatest speed in an ideal gas, an analogy previously drawn by C.F. Barenghi in [26].

4.4 Diffusion of Point Vortices with Multiple Circulation

Although vortices in superfluids with circulation other than $\pm h/m$ are unstable and decay into a number of vortices with $\pm h/m$ circulation [27], there is still interest in how such vortices would behave and diffuse - whether a direct relation between the quantum of circulation and the diffusion coefficient exists is an open question. Solutions to the GPE exhibit this decay, but in the PVM vortices are persistent, and simulating larger circulations is a simple matter of inputting larger values of Γ to the model.

There are a number of caveats to our results in this section: we have used 20 realisations for $\Gamma = \pm 2$, and 30 realisations for $\Gamma = \pm 3$, so have less reliable data which may still exhibit transient effects from individual simulations. Because larger circulation leads to larger velocities, the numerical issues mentioned in Sec. 2.2 are amplified, and so the Hamiltonian is not as well conserved. We halve the step size h for the realisations using $\Gamma = \pm 3$ to reduce this effect. We present summary statistics for the absolute relative change in the Hamiltonian, $|\Delta H_R|$ in Table 4.2.

Regardless of this, we can present some preliminary results on the relation between vortex circulation and diffusion. In Fig. 4.15 we examine the proportion of vortices identified as pairs to ensure we have a reasonable amount of data on the main group to work with.

$ \Gamma $	h	NR	Min	Max	Mean	σ	Q_1	Q_2	Q_3
1	10^{-2}	400	0.0107	0.0261	0.0151	0.00252	0.0134	0.0146	0.0167
2	10^{-2}	20	0.0169	0.0347	0.0222	0.00440	0.0188	0.0220	0.0247
3	5×10^{-3}	30	0.0164	0.0265	0.0204	0.00371	0.0174	0.0238	0.0246

Table 4.2: Summary statistics of the values for $|\Delta H_R|$ at the final time step of our simulations. Here only σ refers to the standard deviation in the absolute relative change in the Hamiltonian, not the standard deviation of the Gaussian functions fitted elsewhere. Q_1 , Q_2 and Q_3 denote the first, second and third quartiles, and NR denotes the number of realisations for the particular choice of circulation $|\Gamma|$ and step size h .

With reference to the analogy drawn between the speed-distribution of vortices and the Maxwell-Boltzmann distribution in the previous section, it may be of interest to note that pairs are formed at a higher initial rate, and the final proportion of vortices that have formed dipoles by the end of the simulations is somewhat greater, for larger magnitude circulation. As larger magnitude circulation leads to greater speeds in a system such systems have higher energy; this can readily be seen from the form of the autonomous Hamiltonian in infinite and periodic domains in (3.1-2). This could be interpreted as more evaporation occurring in systems with higher energy, as we see with an evaporating liquid in a classical context.

Returning to the x -distribution of vortices in the main group, we perform the same analysis as in Sec. 4.3.2. We show the mean values of σ^2 for the Gaussian functions fitted in Fig. 4.16.

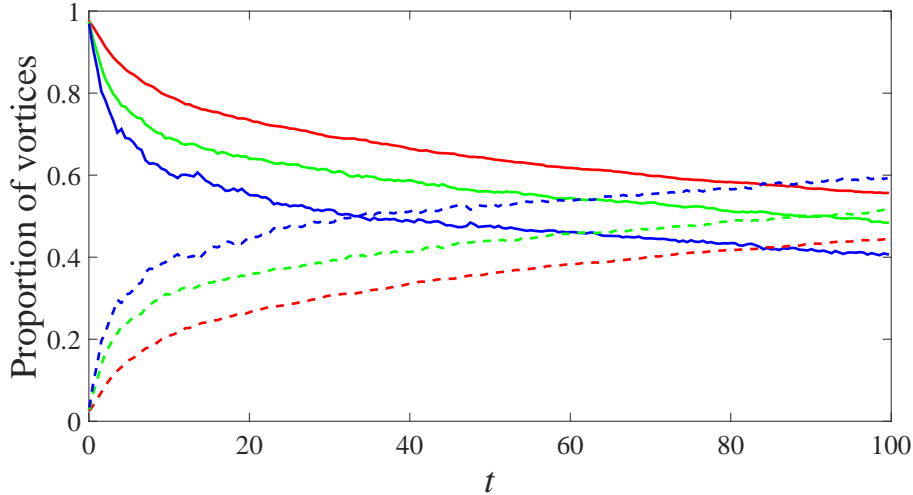


Figure 4.15: Proportion of vortices identified as pairs (dashed lines), and not identified as pairs (solid lines), for simulations using $\Gamma = \pm 1$ (red), $\Gamma = \pm 2$ (green), and $\Gamma = \pm 3$ (blue).

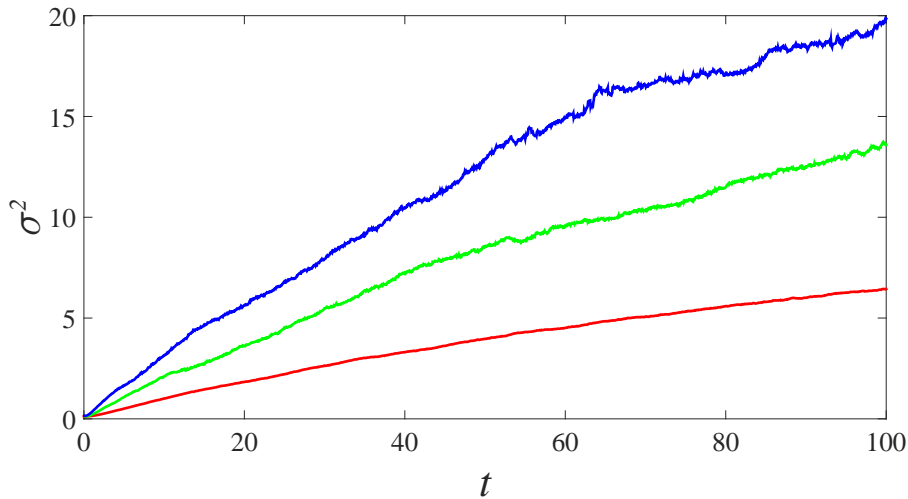


Figure 4.16: Mean variance of fitted Gaussians for $\Gamma = \pm 1$ (red), $\Gamma = \pm 2$ (green), and $\Gamma = \pm 3$ (blue).

From Fig. 4.16, it is apparent that vortices with larger circulation spread out more. To quantify this, we again fit functions of the form:

$$f(t) = \frac{2D_0 t^{\alpha+1}}{(\alpha+1)t_0^\alpha}$$

to our data, as well as to 1 standard deviation above and below. We summarise this in Table 4.3, referring to the parameters found as α_+ , $D_{0,+}$, $t_{0,+}$ and α_- , $D_{0,-}$, $t_{0,-}$ for $\boldsymbol{\mu} + \boldsymbol{\varsigma}$ and $\boldsymbol{\mu} - \boldsymbol{\varsigma}$ for 1 standard deviation above and 1 standard deviation below respectively. Note that the + and - relate to the standard deviation above or below the data, they do not imply any expectation of a larger or smaller value for a parameter.

	$\Gamma = \pm 1$	$\Gamma = \pm 2$	$\Gamma = \pm 3$
α_+	-0.2405	-0.2053	-0.2813
α	-0.2318	-0.2306	-0.2517
α_-	-0.2111	-0.2963	-0.1684
$D_{0,+}$	0.0933	0.2157	0.2656
D_0	0.0688	0.1449	0.1653
$D_{0,-}$	0.0461	0.0974	0.0823
$t_{0,+}$	1.6547	0.7828	1.7886
t_0	1.3500	1.2731	2.3407
$t_{0,-}$	0.6686	1.2075	2.4047

Table 4.3: Parameter values found fitting to $\boldsymbol{\mu}$ and $\boldsymbol{\mu} \pm \boldsymbol{\varsigma}$, as defined in Sec. 4.3.2, for our data using $\Gamma = \pm 1$, $\Gamma = \pm 2$, $\Gamma = \pm 3$.

We do not have enough data to make conclusions about the relation between α and $|\Gamma|$, that is how the rate of diffusion changing varies with the circulation of the vortices, but the values found in Table 4.3 for the mean vectors suggest that α may be unaffected by the absolute circulation of the vortices. We are also interested in how the rate of diffusion changes with the circulation. Recall the form of the diffusion coefficient (4.2) in our solution to the non-standard diffusion equation in one dimension. D_0 and t_0 are constants that scale the diffusion coefficient, so we calculate the value of D_0/t_0^α for the parameters found in Table 4.3.

	$\Gamma = \pm 1$	$\Gamma = \pm 2$	$\Gamma = \pm 3$
$D_{0,+}/t_{0,+}^{\alpha_+}$	0.1053	0.2051	0.3128
D_0/t_0^α	0.0738	0.1532	0.2048
$D_{0,-}/t_{0,-}^{\alpha_-}$	0.0423	0.1030	0.0954

Table 4.4: Values for D_0/t_0^α calculated from values for D_0 , t_0 and α given in Table 4.3.

Again, we do not have enough data at this point to draw conclusions, but the values of D_0/t_0^α found for the mean vectors, given in Table 4.4, are suggestive of a proportional relation between D_0/t_0^α and $|\Gamma|$; that is the rate of diffusion scales with the absolute circulation of the vortices in the system.

Chapter 5

Conclusions & Future Work

5.1 Conclusions

The point vortex model predicts that a collection of quantum vortices in a two-dimensional condensate will spread out in two ways: the formation and rapid escape of vortex dipoles, and the spreading of the remaining vortices through a subdiffusion process. There is an intuitive explanation as to why the rate of diffusion should decrease: the motion of a vortex is not driven by itself, but by the vortices around it, with the magnitude of the velocity contribution of another vortex inversely proportional to the distance between them. If vortices begin to spread out, then the distances between them increase, and so their speeds decrease, slowing their spread.

We find the exponent α governing this subdiffusion process to be in the region of $\alpha \in (-0.2111, -0.2405)$ for vortices with unit magnitude circulation. For vortices with larger circulation, the analysis of our data suggests that the exponent governing the process may be independent of the magnitude of the circulation, though the overall rate of diffusion may be proportional to the magnitude of the circulation.

There may be a deep connection between the formation of vortex dipoles and the diffusion of the main group, which is captured by the Hamiltonian description of the dynamics. We generate a circular distribution of vortices in the infinite plane, half with positive unit circulation and half with negative unit circulation, and calculate the autonomous Hamiltonian of the system, which we call H_0 . We then increase the separation between all vortices by scaling their (x,y) coordinates and calculate the autonomous Hamiltonian for this scaled system, H_S . Doing so for a range of scaling factors, we summarise this in Fig. 5.1. It is clear from this figure that more spread out versions of a system have more energy. We can formalise this by considering the formula for the autonomous Hamiltonian:

$$H_0 = -\frac{1}{4\pi} \sum_{i=1}^n \sum_{j=1}^{n'} \Gamma_i \Gamma_j \ln r_{ij}.$$

If we scale x and y positions of the vortices by a factor of $S \in \mathbb{R}$, then $r_{ij} \rightarrow Sr_{ij}$, and so:

$$H_S = -\frac{1}{4\pi} \sum_{i=1}^n \sum_{j=1}^{n'} \Gamma_i \Gamma_j \ln Sr_{ij}$$

$$\begin{aligned}
&= -\frac{1}{4\pi} \sum_{i=1}^n \sum_{j=1}^n \Gamma_i \Gamma_j [\ln r_{ij} + \ln S] \\
&= H_0 - \frac{1}{4\pi} \sum_{i=1}^n \sum_{j=1}^n \Gamma_i \Gamma_j \ln S.
\end{aligned}$$

The $\Gamma_i \Gamma_j$ factors are $+1$ if $\Gamma_i = \Gamma_j$ and -1 if $\Gamma_i \neq \Gamma_j$. As there are an equal number of positive vortices and negative vortices these terms would all cancel if it were not for the omission of the $i = j$ terms; instead we find:

$$H_S = H_0 + \frac{n \ln S}{4\pi}.$$

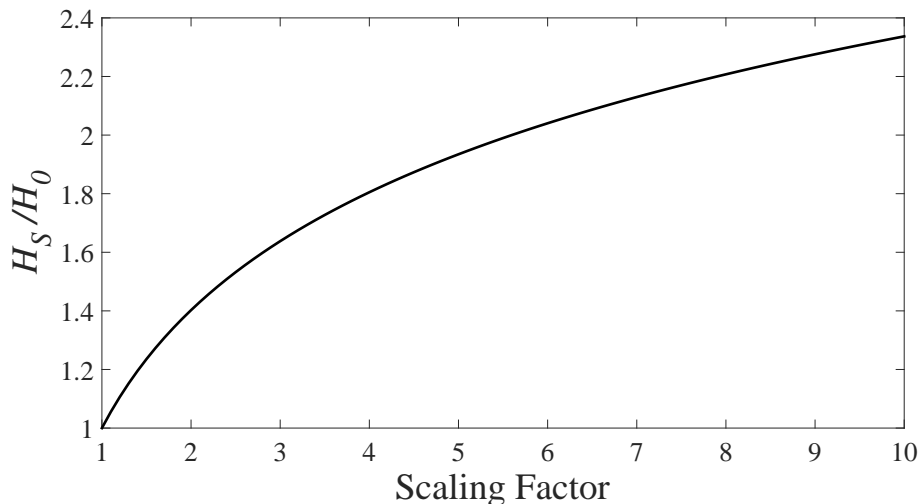


Figure 5.1: Increase in the value of the Hamiltonian as the separation within a system is increased. This curve uses one configuration, which is then scaled, but is representative of the general effect of increasing the separation uniformly within a system of point vortices.

As the vortices in our model follow trajectories defined by the Hamiltonian, it is reasonable to expect that in order for some vortices to spread out other vortices must move closer together, with some forming dipoles, although we offer no formal proof of this.

5.2 Future Work

Our next objective is to improve the numerical accuracy of our simulations. We intend to do this by two means, firstly by considering higher order time-adaptive Runge-Kutta-Fehlberg and related methods. A number of these are available to us, so before performing a large number of simulations with one method we will analyse the efficiency of a selection of methods in terms of the number of function evaluations required

to attain particular levels of conservation of the Hamiltonian for our particular model. Additionally, although we have previously used a standard point vortex velocity profile, we will investigate the separation of vortices of identical circulation at which non-negligible numerical errors occur, and consider imposing a Rankine vortex profile with a suitable core size based on this information.

Having made these adjustments, we aim to produce more realisations of our simulations, in particular those with larger values of circulation, in order to establish more reliable results and a more precise relationship between the circulation of vortices and the diffusion process they exhibit. We also intend to dedicate some time to refining the identification of vortex dipoles; although the effects of misclassified vortices on the distribution should be negligible over a large number of runs, there are no detrimental effects anticipated, except perhaps a miniscule increase in processing time required, and the technique may be useful in other similar simulations.

In this report we have focused our analysis on the main group, however we already have a lot of data on the vortex dipoles and will be generating more. We are keen to investigate the relation between the energy of the system, and the formation of pairs and their velocity distribution.

For comparison with the results concerning the diffusion of the main group obtained using the point vortex model, we will produce numerical solutions to the Gross-Pitaevskii equation in two-dimensions. Here we are not interested in dipoles once they move away from the main group, so can remove them using the ‘unwinding’ technique discussed in [28] once their separation from the main cluster becomes such that their contribution to the velocity field within the group becomes negligible. This will allow us to simulate a smaller region than would otherwise be necessary, saving a great deal of computational resources.

We then plan to expand our research into three-dimensions, using both the vortex filament model based on the Biot-Savart law to investigate the broad dynamics, and the Gross-Pitaevskii equation in 3 dimensions to explore the effects of phonon emission, vortex-antivortex annihilation, and other effects not modelled by the point vortex model or the vortex filament model.

Appendix A

Butcher Tableaux of Selected Runge-Kutta Methods

0				
$\frac{1}{2}$	$\frac{1}{2}$			
$\frac{1}{2}$	0	$\frac{1}{2}$		
1	0	0	1	
<hr/>				
	$\frac{1}{6}$	$\frac{1}{3}$	$\frac{1}{3}$	$\frac{1}{6}$

Table A.1: Coefficients, weights and nodes for the original 4th-order Runge-Kutta method.

0								
$\frac{1}{10}$	$\frac{1}{10}$							
$\frac{2}{9}$	$\frac{-2}{81}$	$\frac{20}{81}$						
$\frac{3}{7}$	$\frac{615}{1372}$	$\frac{-270}{343}$	$\frac{1053}{1372}$					
$\frac{3}{5}$	$\frac{3243}{5500}$	$\frac{-54}{55}$	$\frac{50949}{71500}$	$\frac{4998}{17875}$				
$\frac{4}{5}$	$\frac{-26492}{37125}$	$\frac{72}{55}$	$\frac{2808}{23375}$	$\frac{-24206}{37125}$	$\frac{338}{459}$			
1	$\frac{5561}{2376}$	$\frac{-35}{11}$	$\frac{-24117}{31603}$	$\frac{899983}{200772}$	$\frac{-5225}{1836}$	$\frac{3925}{4056}$		
1	$\frac{465467}{266112}$	$\frac{-2945}{1232}$	$\frac{-5610201}{14158144}$	$\frac{10513573}{3212352}$	$\frac{-424325}{205632}$	$\frac{376225}{454272}$	0	
<hr/>								
	$\frac{61}{864}$	0	$\frac{98415}{321776}$	$\frac{16807}{146016}$	$\frac{1375}{7344}$	$\frac{1375}{5408}$	$\frac{-37}{1120}$	$\frac{1}{10}$

Table A.2: Coefficients, weights and nodes for a 6th-order method introduced by P. J. Prince & J. R. Dormand in [29]

Bibliography

- [1] NASA. Jupiter's Great Red Spot Region. http://www.nasa.gov/mission_pages/juno/multimedia/pia00065.html. [Online; accessed 27-April-2015].
- [2] H. Kellay. Soap bubbles for predicting cyclone intensity? <http://phys.org/news/2014-01-soap-cyclone-intensity.html>. [Online; accessed 27-April-2015].
- [3] P.G. Tait. On the integrals of the hydrodynamical equations which express vortex motions (English translation of Helmholtz' 1858 paper). *Philos. Mag.*, 33 (Suppl.).
- [4] M. Zwiernik. BEC Vortices. https://www.learner.org/courses/physics/visual/visual.html?shortname=vortex_image. [Online; accessed 27-April-2015].
- [5] S. Middelkamp et al. Guiding-center dynamics of vortex dipoles in Bose-Einstein condensates. *Phys. Rev. A*, 84, Jul 2011.
- [6] C.J. Pethick and H. Smith. *Bose-Einstein condensation in dilute gases*, p. 166. Cambridge, second edition, 2008.
- [7] L. Erdős, B. Schlein, and H.-T. Yau. Rigorous derivation of the Gross-Pitaevskii equation. *Phys. Rev. Lett.*, 98, Jan 2007.
- [8] B. Jackson, J.F. McCann, and C.S. Adams. Dissipation and vortex creation in bose-einstein condensed gases. *Phys. Rev. A*, 61, Apr 2000.
- [9] C. Rorai, K.R. Sreenivasan, and M.E. Fisher. Propagating and annihilating vortex dipoles in the Gross-Pitaevskii equation. *Phys. Rev. B*, 88, Oct 2013.
- [10] W. Bao, D. Jaksch, and P.A. Markowich. Numerical solution of the Gross-Pitaevskii equation for Bose-Einstein condensation. *J. Comput. Phys.*, 187, May 2003.
- [11] F. Piazza. *Ultracold Bosonic Gases: Superfluidity and Quantum Interferometry*. PhD thesis, University of Trento, 2011.
- [12] H. Aref. Point vortex dynamics: A classical mathematics playground. *Journal of Mathematical Physics*, 48(6), 2007.
- [13] P.G. Saffman. *Vortex Dynamics*. Cambridge University Press, first corrected edition, 1995.
- [14] H. von Helmholtz. Über integrale der hydrodynamischen gleichungen, welche den wirbelbewegungen entsprechen. *Crelle*, 55, 1858.

- [15] D.B. Gaiotti and F. Stel. The Rankine vortex model. *PhD course on Environmental Fluid Mechanics-ICTP/University of Trieste*, 2006.
- [16] A. Korzybski. *Science and sanity: an introduction to non-Aristotelian systems and general semantics*. Lancaster, 1933.
- [17] M.W. Kutta. Beitrag zur näherungsweise integration totaler differentialgleichungen. *Zeitschrift für Mathematik und Physik*, 46, 1901.
- [18] J.I. Palmore. Relative equilibria of vortices in two dimensions. *Proceedings of the National Academy of Sciences*, 79, 1982.
- [19] E. Fehlberg. New high-order Runge-Kutta formulas with stepsize control for systems of first- and second-order differential equations. *Z. angew. Math. Mech*, 44, 1964.
- [20] E. Fehlberg. New high-order Runge-Kutta formulas with an arbitrarily small truncation error. *Z. angew. Math. Mech*, 46, 1966.
- [21] E. Fehlberg. Classical fifth-, sixth-, seventh-, and eighth-order Runge-Kutta formulas with stepsize control. Technical Report R-287, NASA, 1968.
- [22] E. Fehlberg. Low-order classical Runge-Kutta formulas with stepsize control and their application to some heat transfer problems. Technical Report R-315, NASA, 1969.
- [23] G.R. Kirchhoff. *Vorlesungen über mathematische Physik. Mechanik*. Leipzig, 1876.
- [24] R. Gorenflo et al. Time fractional diffusion: a discrete random walk approach. *Nonlinear Dynamics*, 29, Jul 2002.
- [25] Mathworks. Matlab R2015a Documentation. <http://uk.mathworks.com/help/matlab/ref/fminsearch.html>. [Online; accessed 27-April-2015].
- [26] C.F. Barenghi and D.C. Samuels. Evaporation of a packet of quantized vorticity. *Phys. Rev. Lett.*, 89, Sept 2002.
- [27] M. Möttönen et al. Splitting of a doubly quantized vortex through intertwining in Bose-Einstein condensates. *Phys. Rev. A*, 68, Aug 2003.
- [28] M.T. Reeves et al. Identifying a superfluid Reynolds number via dynamical similarity. *Phys. Rev. Lett.*, 114, Apr 2015.
- [29] P.J. Prince and J.R. Dormand. High order embedded Runge-Kutta formulae. *Journal of Computational and Applied Mathematics*, 7(1):67–75, Mar 1981.